
A MULTISCALE SPATIOTEMPORAL APPROACH FOR SMALLHOLDER IRRIGATION DETECTION

Terence Conlon*

Department of Mechanical Engineering
Columbia University
New York, NY, USA
terence.conlon@columbia.edu

Christopher Small

Lamont Doherty Earth Observatory
Columbia University
Palisades, NY, USA
csmall@columbia.edu

Vijay Modi

Department of Mechanical Engineering
Columbia University
New York, NY, USA
modi@columbia.edu

March 21, 2022

ABSTRACT

In presenting an irrigation detection methodology that leverages multiscale satellite imagery of vegetation abundance, this paper introduces a process to supplement limited ground-collected labels and ensure classifier applicability in an area of interest. Spatiotemporal analysis of MODIS 250m Enhanced Vegetation Index (EVI) timeseries characterizes native vegetation phenologies at regional scale to provide the basis for a continuous phenology map that guides supplementary label collection over irrigated and non-irrigated agriculture. Subsequently, validated dry season greening and senescence cycles observed in 10m Sentinel-2 imagery are used to train a suite of classifiers for automated detection of potential smallholder irrigation. Strategies to improve model robustness are demonstrated, including a method of data augmentation that randomly shifts training samples; and an assessment of classifier types that produce the best performance in withheld target regions. The methodology is applied to detect smallholder irrigation in two states in the Ethiopian highlands, Tigray and Amhara, where detection of irrigated smallholder farm plots is crucial for energy infrastructure planning. Results show that a transformer-based neural network architecture allows for the most robust prediction performance in withheld regions, followed closely by a CatBoost random forest model. Over withheld ground-collection survey labels, the transformer-based model achieves 96.7% accuracy over non-irrigated samples and 95.9% accuracy over irrigated samples. Over a larger set of samples independently collected via the introduced method of label supplementation, non-irrigated and irrigated labels are predicted with 98.3% and 95.5% accuracy, respectively. The detection model is then deployed over Tigray and Amhara, revealing crop rotation patterns and year-over-year irrigated area change. Predictions suggest that irrigated area in these two states has decreased by approximately 40% from 2020 to 2021.

Keywords irrigation detection · spatiotemporal modeling · multiscale imagery · machine learning · Ethiopia

1 Introduction

Between 1970 and 2008, global irrigated area increased from 170 million to 304 million hectares [Vogels et al., 2019a]. In sub-Saharan Africa however, as little as 4-6% of cultivated area is irrigated, given the lack of electric grid

*Corresponding author

infrastructure and the high cost of diesel [Wiggins et al., 2021]. Locating isolated irrigation identifies areas that can support higher quality energy provision services – e.g. a grid connection or minigrid installation – as these sites can sustain higher energy demands and the attendant electricity costs [Conlon et al., 2020]. Facilitated through informed planning, irrigation expansion has a direct impact on poverty reduction: In Ethiopia, one study found that the average income of irrigating households was double that of non-irrigating households [Gebregziabher et al., 2009].

In data poor locations, satellite imagery provides a source of detailed synoptic observations of irrigated agriculture [Pervez et al., 2014]. A previous irrigation mapping effort in Ethiopia used three 1.5m resolution SPOT6 images to distinguish between large-scale and smallholder irrigation in the Ethiopian rift [Vogels et al., 2019a]. This approach was then adapted to intake a timeseries of 10m Sentinel-2 imagery to predict irrigation presence across the horn of Africa [Vogels et al., 2019b]. While both studies demonstrated high accuracies over collected observations, limited labels precluded a more rigorous performance assessment over the entire area of interest. Other studies have used multiscale imagery to detect irrigation, including one that fuses MODIS and Landsat imagery to identify irrigated extent, frequency, and timing in northwestern China [Chen et al., 2018]. Here, unique advantages of satellite imagery products at different resolutions are exploited: 250m MODIS imagery is valuable for characterizing vegetation over large areas [Huete et al., 1999], while decameter resolution imagery from Landsat or Sentinel-2 missions can better discern plot extent [Phiri et al., 2020].

Deep learning techniques have become widely used for land process classification, as they uncover intricate structures in large, complex datasets [Lecun et al., 2015]; and provide a robust method of handling phenological variability [Zhong et al., 2019]. However, despite increasing availability of remotely sensed imagery, computing resources, and advanced algorithms for information extraction, high-quality labels remain scarce and expensive to acquire. Methods of overcoming label scarcity generally fall into one of four categories: 1) using pretrained networks; 2) unsupervised and self-supervised learning; 3) data augmentation; or 4) additional label collection [Li et al., 2018]. Even as pretrained networks like ImageNet [Deng et al., 2009] are highly effective for true-color image classification, these networks' weights do not translate to tasks that intake multispectral or hyperspectral imagery [Tao et al., 2020]. Unsupervised learning techniques, including those that ensemble different clustering methods – e.g. Banerjee et al. [2015] – have been shown to effectively organize unlabeled imagery. Existing work has also demonstrated that training a Generative Adversarial Network (GAN) – itself a type of unsupervised learning – has allowed for improved change detection performance on multispectral imagery, e.g. Saha et al. [2019]. For data augmentation, three techniques are often implemented: image translation, rotation, and flipping [Yu et al., 2017, Stivaktakis et al., 2019]; however, these techniques do not have obvious analogues for pixel-based classification.

In assessing the impact of training dataset size on land cover classification performance, Ramezan et al. [2021] finds that investigating multiple types of classifiers is recommended, as the performance of specific classifiers is highly dependent on the number of training samples. A number of other studies have introduced methods for obtaining training samples, including collection via hand-engineered rules [Abbas et al., 2015]; normalized difference in vegetation index (NDVI) thresholding [Bazzi et al., 2021]; finding neighboring pixels that are highly similar to labeled pixels [Naik and Kumar, 2021]; and visual inspection of high-resolution [Vogels et al., 2019b] and decameter resolution [Wu and Chin, 2016] imagery. Lastly, while larger training datasets generally yield better model performance, condensing input samples via dimensionality reduction has been demonstrated to increase land cover classification accuracy [Sivaraj et al., 2022, Stromann et al., 2020].

Another lingering issue in land process mapping is determining the conditions under which a model can be utilized in locations beyond where it was trained. Site-specific methods may not be easily transferable to other places or climates [Ozdogan et al., 2010, Bazzi et al., 2020], and the performance of transferred models can often only be assessed *after* full implementation in a novel setting [de Lima and Marfurt, 2020]. Therefore, processes that yield insights about model transferability *before* training and inference offer benefits to researchers seeking to understand the maximum spatial applicability of their approaches.

As current methods primarily focus on already well-understood areas of interest with existing datasets, new techniques and products need to be developed for parts of the world lacking labeled data. In the realm of irrigation detection, new methodologies and mapping products can help identify locations for further energy system planning and investment, as these areas contain latent energy demands that can make higher quality energy services cost-effective and increase incomes. To this end, the following manuscript presents a multiscale methodology that leverages 250m MODIS imagery for regional phenological characterization and 10m Sentinel-2 imagery for irrigation detection on smallholder plots. This approach is then applied to the 205,000 km² Ethiopian highlands, whereby it introduces a novel method of label collection; an evaluation of different classifier architectures and training strategies that ensure model applicability within the area of interest; and an assessment of irrigated area in the Tigray and Amhara states of Ethiopia for 2020 and 2021.

2 Background

Identification of dry season greening as potentially irrigated agriculture must take into account spatiotemporal variations in native vegetation phenological cycles. The complex topography of the Ethiopian Highlands and East African rift system, combined with the latitudinal movement of the InterTropical Convergence Zone (ITCZ) and seasonal upwelling of the Somali current in the Arabian Sea produces a diversity of rainfall patterns that control annual vegetation phenological cycles in the study area². In order to provide phenological context with which to identify anomalous dry season greening, a regional vegetation phenology map is derived from spatiotemporal analysis of timeseries of vegetation abundance maps. Using the spatiotemporal characterization and temporal mixture modeling approach given by [Small, 2012] applied to timeseries of MODIS enhanced vegetation index (EVI) maps, four temporal endmember (tEM) phenologies are identified that bound the temporal feature space of all vegetation phenology cycles observed on the East African Sahel. These four tEM phenologies form the basis of a linear temporal mixture model that can be inverted to provide tEM fraction estimates for each pixel's vegetation phenology. Figure 1 presents a spatiotemporal phenological characterization for the country, created from 16-day 250m MODIS EVI imagery between June 1st, 2011 and June 1st, 2021.

The four tEMs extracted for Ethiopia are as follows: a *single cycle* tEM, representing a single annual vegetation cycle per year that peaks in September/October; an *evergreen* tEM, representing perennial vegetation; a *double cycle* tEM, representing semiannual vegetation cycles observed on the Somali peninsula; and a *non-vegetated* tEM, representing barren or non-existent vegetation. The ensuing phenology map in Figure 1 contains unmixing root mean square (RMS) error less than 10% for 90% of the pixels; additional unmixing error statistics and the locations of the extracted tEMs in principal component (PC) feature space are shown in Supplementary Figures S1-S2.

Figure 1 roughly divides into 4 quadrants. In the northeast quadrant, Afar appears as dark green, indicating that none of the 4 tEMs contribute significantly to phenologies in this part of the country: The vegetation that does exist in this mostly barren area is represented by low levels of evergreen tEM abundances. In the southeast quadrant, dominated by Somali and a portion of Oromia, vegetation patterns cycle twice annually. This is an area with bimodal rainfall but low total annual precipitation that results in the *double cycle* tEM containing peak vegetation abundances lower than those of the *single cycle* and *evergreen* tEMs. It follows that southeast Ethiopia is more pastoral with sparser vegetation than other parts of the country.

The southwest quadrant – covering Southern Nations, Nationalities, and Peoples' (SNNP) Region, Sidama, and the western portion of Oromia – contains significant amounts of evergreen vegetation, as is demonstrated by its bright green hue. Here, evergreen vegetation is supported by bimodal rainfall with higher levels of annual precipitation than in eastern Ethiopia. In contrast, the northwest quadrant of the phenology map contains red-dominant color gradients, indicating phenologies similar to the *single cycle* tEM. This portion of the country, known as the Ethiopian highlands and comprising of Amhara and Tigray, is highly agricultural; the main cropping season lasts from June to October and coincides with the primary *kiremt* rains, with some secondary cropping following the lighter *belg* rains from March to May. Accordingly, cropping that occurs during the dry season between November and March is likely to be irrigated.

In presenting a map of dominant vegetation phenologies in Ethiopia, Figure 1 provides a guide for land cover classification applicability within the country. For instance, a dry season irrigation detector trained in Amhara will perform poorly in SNNP, as phenological patterns differ significantly across these states, and dry season crop cycles exhibit different vegetation signatures. In contrast, a dry season irrigation detector developed across Amhara can be transferred to Tigray or Benishangul-Gamuz, due to regional phenological similarities.

The named, italicized outlines in Figure 1 represent the 8 areas containing labels used in this manuscript, referred to as *regions*: The yellow outline indicates a region where labels were collected via a ground survey, and the purple outlines indicate regions where labels were collected by means of visual interpretation and timeseries inspection. Full information on the labeled data collection process is presented in Section 3.

3 Materials and Methods

The data collection portion of this manuscript's methodology consists of pairing Sentinel-2 imagery with labeled polygons to train an irrigation detector. Here, a pixel timeseries paired with a binary irrigation/non-irrigation label constitutes a sample. Irrigation is defined as such: A pixel is irrigated if its phenology includes at least one non-perennial vegetation cycle during the dry season, December 1st to April 1st for the Ethiopian highlands. Conversely, a pixel is non-irrigated if its phenology demonstrates only vegetation growth that can be attributed to the area's known rainy

²See Wakjira et al. [2021] for a fuller discussion of rainfall patterns in Ethiopia.

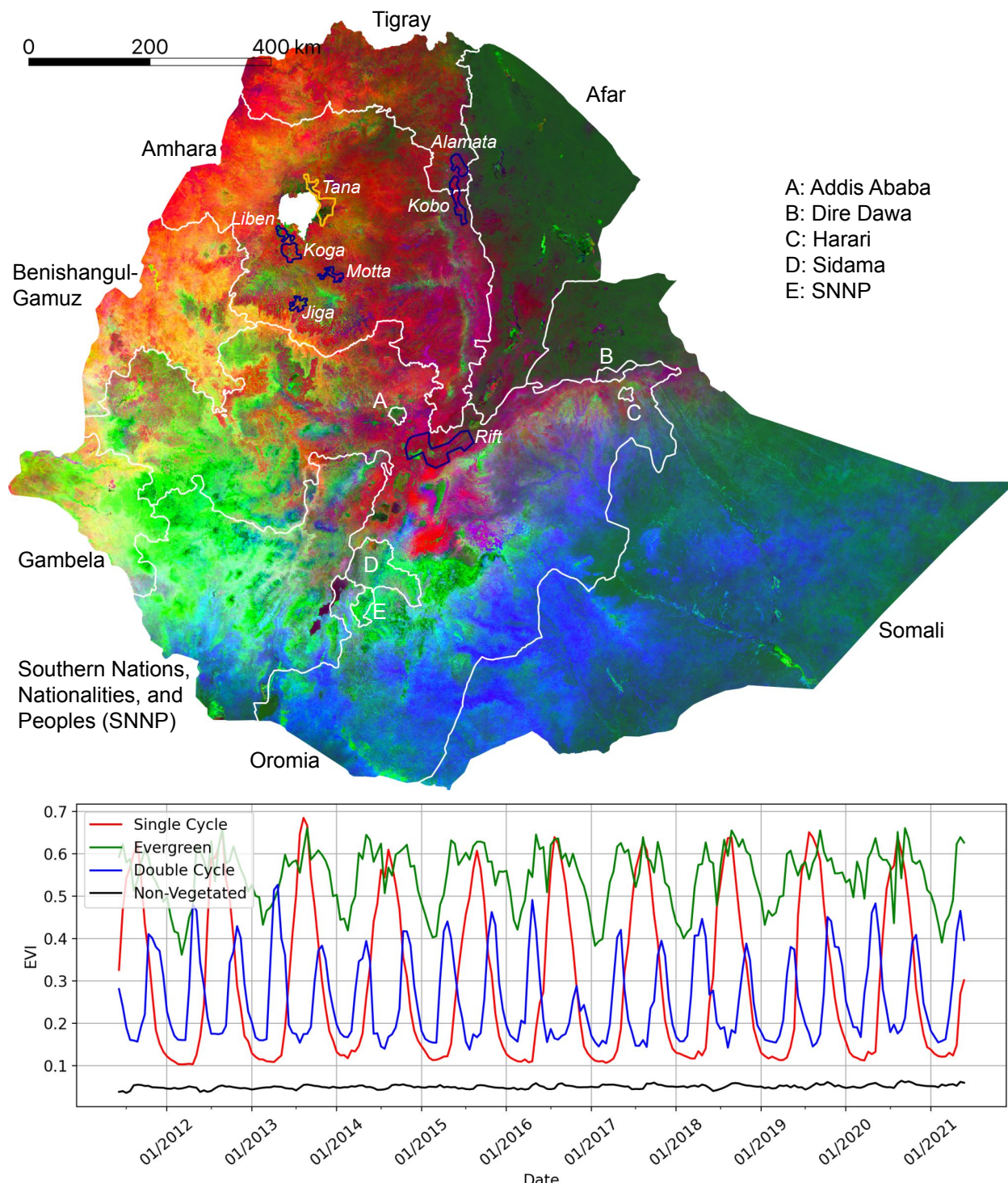


Figure 1: Continuous endmember fraction map derived from a temporal mixture model of 250m MODIS enhanced vegetation indices (EVI). Smooth gradients and abrupt transitions in phenology are primarily related to topography and variations in precipitation. Region names showing locations of labeled polygons are italicized: The region containing ground collection (GC) labels is delineated in gold; the regions containing visual collection (VC) labels are delineated in blue.

seasons. Irrigated areas are only of interest if they contain dry season vegetation cycles; this strict definition of irrigation excludes supplemental irrigation practices and perennial crops that may be consistently irrigated throughout the year.

3.1 Sentinel-2 imagery collection

The following analysis uses bottom-of-atmosphere corrected (processing level L2A) Sentinel-2 temporal stacks – four dimensional arrays created by stacking a set spatial extent of imagery bands over multiple timesteps – using the Descartes Labs (DL) platform, a commercial environment for planet-scale geospatial analysis. Images are collected at a 10-day time resolution. To focus on the 2020 and 2021 dry seasons, the time period of interest is defined as between June 1st, 2019, and June 1st, 2021. Given the 10-day timestep, 72 image mosaics are collected – 36 per year. Additional information on the imagery download process is available in the Supplementary Materials.

3.2 Label collection

Two types of labeled data are leveraged for irrigation mapping: *ground collection* (GC) labels, acquired via an in-person survey; and *visual collection* (VC) labels, acquired via visual identification of dry season vegetation from Sentinel-2 imagery using the DL platform and subsequent cleaning via timeseries clustering. The locations of these GC and VC regions are shown in italics in Figure 1, with all labels collected for the 2021 dry season. A description of the ground collection survey is presented in the Supplementary Materials. As the GC labels constitute our highest quality irrigation observations, verified by in situ visits to individual plots, we do not use them for training during the model sensitivity analysis, instead reserving them for validation of classifier performance.

3.2.1 Visual label collection

To supplement the GC labels located in Tana, visually collected labels are acquired for seven separate regions via a three-step process of 1) visual inspection, 2) EVI timeseries confirmation, and 3) cluster cleaning. Each of these steps is described in its eponymous subsection below.

Visual inspection The first step in the VC labeling process involves drawing polygons around locations that either: a) present as cropland with visible vegetation growth (for the collection of irrigated samples), or b) present as cropland with no visible vegetation growth (for the collection of non-irrigated samples), based on dry-season, false-color Sentinel-2 imagery presented on the DL platform. Sub-meter resolution commercial satellite imagery from Google Earth Pro is also used to confirm the existence of cropland in the viewing window. For the collection of non-irrigated labels, polygons are restricted to areas that contain non-perennial cropland; however, because only phenologies that contain dry season vegetation cycles are considered irrigated, non-irrigated polygons occasionally overlap other types of land cover – e.g., perennial crops, fallow cropland, or areas with human settlement – with any overlap likely to improve training robustness.

EVI timeseries confirmation After drawing a polygon around a suspected irrigated or non-irrigated area, the second step in the VC label acquisition process entails inspection of the median Sentinel-2 EVI timeseries of all pixels contained within the polygon; this step is shown in the plot windows of Figure 2. Here, all available Sentinel-2 imagery with less than 20% cloud cover between June 1, 2020, and June 1, 2021 is retrieved; a cubic spline is then fit to all available data to generate continuous EVI timeseries. For potential irrigated polygons, if the EVI timeseries shows a clear peak above 0.2 during the dry season, it is confirmed as irrigated. Similarly, for potential non-irrigated polygons, an EVI timeseries that demonstrates a single vegetation cycle attributable to Ethiopia's June to September rains is taken as confirmation of a non-irrigated VC polygon. However, if the EVI timeseries does not confirm the expected irrigated/non-irrigated class, or if the plotted EVI error bars (representing \pm one standard deviation of the EVI values at that timestep) indicate a level of signal noise within the polygon that prevents the identification of a clear vegetation phenology, the polygon is discarded.

Figure 2(a) demonstrates an example of irrigated VC label collection in the Koga region – here, the double vegetation peak present in the EVI timeseries confirms the purple polygon in the center of the window as irrigated (blue polygons indicate areas already saved as irrigated VC labels). Figure 2(b) demonstrates the same process for non-irrigated VC labels, also in Koga: The single EVI peak in October 2020 confirms the pink polygon in the top left of the window as non-irrigated (red polygons indicate areas already saved as non-irrigated VC labels).

Cluster cleaning The third step in the VC label acquisition process involves bulk verification of the collected timeseries by means of cluster cleaning. For each VC region, all pixels that reside within labeled polygons are collected and split based on the irrigated/non-irrigated class labels of the polygons. Fifteen-component Gaussian mixture models

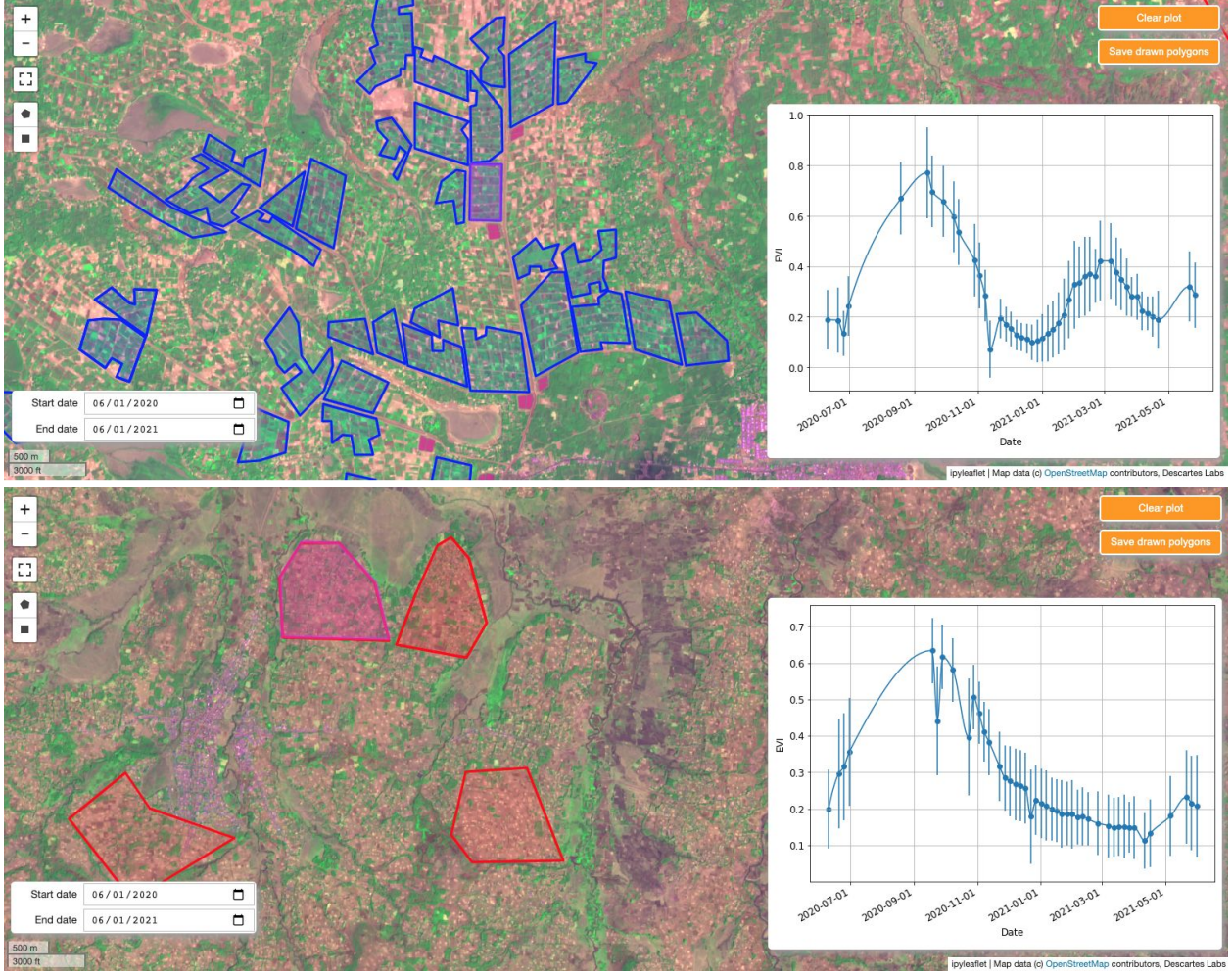


Figure 2: Example of the visual collection (VC) labeling process in Koga using the Descartes Labs platform. Blue polygons denote areas determined to be irrigated; red polygons are determined to be non-irrigated. Background imagery is a false-color Sentinel-2 image taken in March 2021: red, near-infrared, and blue bands are presented in the RGB channels, respectively. In (a), the Sentinel-2 enhanced vegetation index (EVI) timeseries is shown for the drawn purple rectangle in the middle of the window; in (b), the Sentinel-2 EVI timeseries is shown for the drawn pink, semi-octagonal polygon in the top left of the window. Both timeseries present the median EVI values for all pixels contained within the drawn polygon; the error bars show one standard deviation of these values above and below the median. In both figures, the drawn polygons are confirmed as VC labels, since they meet the definitions of irrigation/non-irrigation, respectively.

are fit to each class’s data to extract the dominant phenologies contained within the region’s samples; the EVI timeseries representing the cluster centroids are then plotted, with the plot legend displaying the number of samples per cluster. Figure 3(a) presents the results of this initial clustering for the Koga region.

From the initial cluster timeseries, an iterative process begins to ensure that all cluster timeseries align with the specified class label. For an irrigated cluster timeseries to be kept, it must contain multiple successive EVI values above and below 0.2, and it must contain a clear EVI peak above 0.2 during the dry season. Analogously, non-irrigated cluster timeseries are discarded if they display a clear dry-season EVI peak above 0.2. If these conditions are not met – as is the case for Clusters 3, 6, and 13 of the Koga irrigated samples, which do not contain a clear EVI peak above 0.2 between December 1, 2020 and April 1, 2021 (Clusters 6 and 13) or do not senesce below an EVI threshold of 0.2 for successive timesteps (Cluster 3) – all pixel timeseries associated with that cluster are discarded from the labeled data. This process is repeated until all 15 clusters for both classes demonstrate EVI signals that meet the non-irrigated/irrigated class definitions. The final, cleaned cluster timeseries for the Koga region are shown in Figure 3(b).

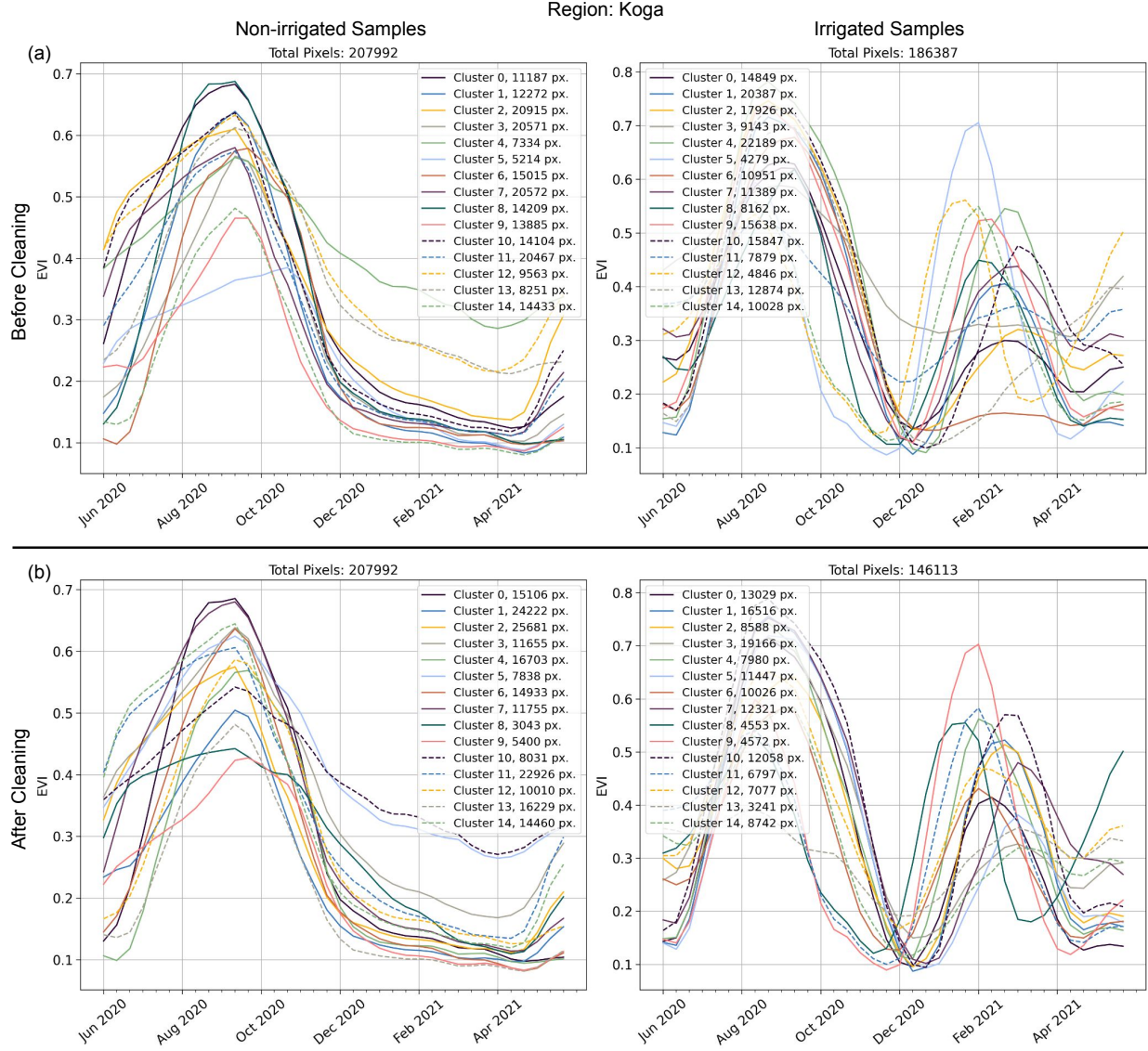


Figure 3: Clustered enhanced vegetation index (EVI) timeseries before and after cluster cleaning for the Koga visual collection (VC) region. Before and after cleaning, pixels are grouped into one of 15 randomly indexed clusters. In (a), Clusters 3, 6, and 13 of the irrigated samples are discarded due to either (6, 13) not containing a clear EVI peak above 0.2 during the dry season (December 1st to April 1st); or (3) not containing successive EVI values below 0.2. All non-irrigated clusters display a single vegetation peak aligned with the main rainy season, and the irrigated clusters after cleaning (b) all display a vegetation cycle during the dry season.

Cluster-cleaning is performed for all regions' labeled data, including labeled data collected from the GC region, Tana. For increased visibility into the labeled data collected and used for training, these regions' clusters before and after cleaning are included in Appendix A of the Supplementary Materials.

A summary of the number of collected polygons and cleaned pixel timeseries samples in each region is shown in Supplementary Tables S2-S3: In total, 1,207,233 non-irrigated samples and 907,887 irrigated samples are used, taken from 1702 and 750 labeled polygons, respectively. For model training and evaluation, data are divided among training, validation, and test splits³. Here, polygons in each labeled region are split according to a 70/15/15 training/validation/test

³In splitting the labeled data, the training/validation/testing terminology standard in machine and deep learning literature is adopted.

Table 1: Prediction admissibility criteria. All criteria need to be satisfied for a prediction to be admitted as irrigated.

Admissibility Criteria	Motivation
10 th percentile of EVI timeseries < 0.2	Remove evergreen pixels
90 th percentile of EVI timeseries > 0.2	Remove barren/non-vegetated pixels
Maximum of the EVI timeseries during the dry season (Dec. 1 – Apr. 1) > 0.2	Remove pixels with no vegetation growth in the dry season
Ratio of the 90 th :10 th percentile of the EVI timeseries > 2	Remove evergreen pixels
Shuttle Radar Topography Mission slope measurement < 8%	Remove pixels in highly sloped settings where cropping is impractical

ratio; this method ensures that highly similar pixels from within the same polygon do not exist across training configurations, a division of data that would artificially inflate model performance for the task of predicting irrigation over pixel timeseries unseen by the model. All training, validation, and testing is performed pixelwise (i.e., having removed the spatial relationships of samples).

The Supplementary Materials contain additional information about the labeled data distributions, including a statistical evaluation of the similarity of labeled samples across region and class (see Supplementary Tables S4-S5)

3.3 Prediction admissibility criteria

Given that irrigated phenologies exist over a small fraction of the total land area of the Ethiopian highlands, and that there are many types of land cover that do not fall within this manuscript’s non-irrigated/irrigated cropland dichotomy, a set of criteria are imposed to exclude pixel phenologies that are not cropland or are highly unlikely to be irrigated. Table 1 presents five criteria that must all be met for a pixel timeseries to be potentially irrigated and the motivation behind each.

These vegetation-specific criteria are informed by the EVI distributions of labeled irrigated samples for all label collection regions: Supplementary Figure S3 contains cumulative distribution functions (CDFs) for the 10th and 90th EVI timeseries percentiles, the 90th:10th EVI timeseries percentile ratio, and the maximum EVI value during the dry season. CDFs are presented for all regions’ irrigated samples, including for a set of polygons collected over evergreen land cover areas.

The criteria in Table 1 are also used to create a reference irrigation classifier that does not rely on machine learning. For this reference classifier, if all 5 conditions are met, the sample is deemed irrigated; if any of the conditions is not satisfied, the sample is deemed non-irrigated.

3.4 Model training

3.4.1 Model architectures

Five separate classifier types are compared to determine the model architecture with the most robust irrigation detection performance across regions. The first two classifiers are decision tree-based: A random forest with 1000 trees [Breiman, 2001]; and a CatBoost model that uses gradient boosting on up to 1000 trees [Dorogush et al., 2017]. The other three classifiers are neural networks (NN): A baseline network, an LSTM-based network, and a transformer-based network. For comparability, these three classifier architectures are designed to have similar structures, based on the strong baseline model structure proposed in [Wang et al., 2017]; as seen in Figure 4, they differ only in the type of encoding blocks used.

3.4.2 Model training strategy

The implemented model training strategy addresses two potential pitfalls among training processes: 1) imbalanced samples across region and class; and 2) high similarity among samples within a region that may not reflect the sample distributions across all regions. Consistent with best practices in dealing with imbalanced data, this first issue is addressed with a) class balancing weights specific to each region, based on the “balanced” heuristic inspired by King and Zeng [2001]; and b) a region-specific weight equal to the ratio of the maximum number of samples in any region to

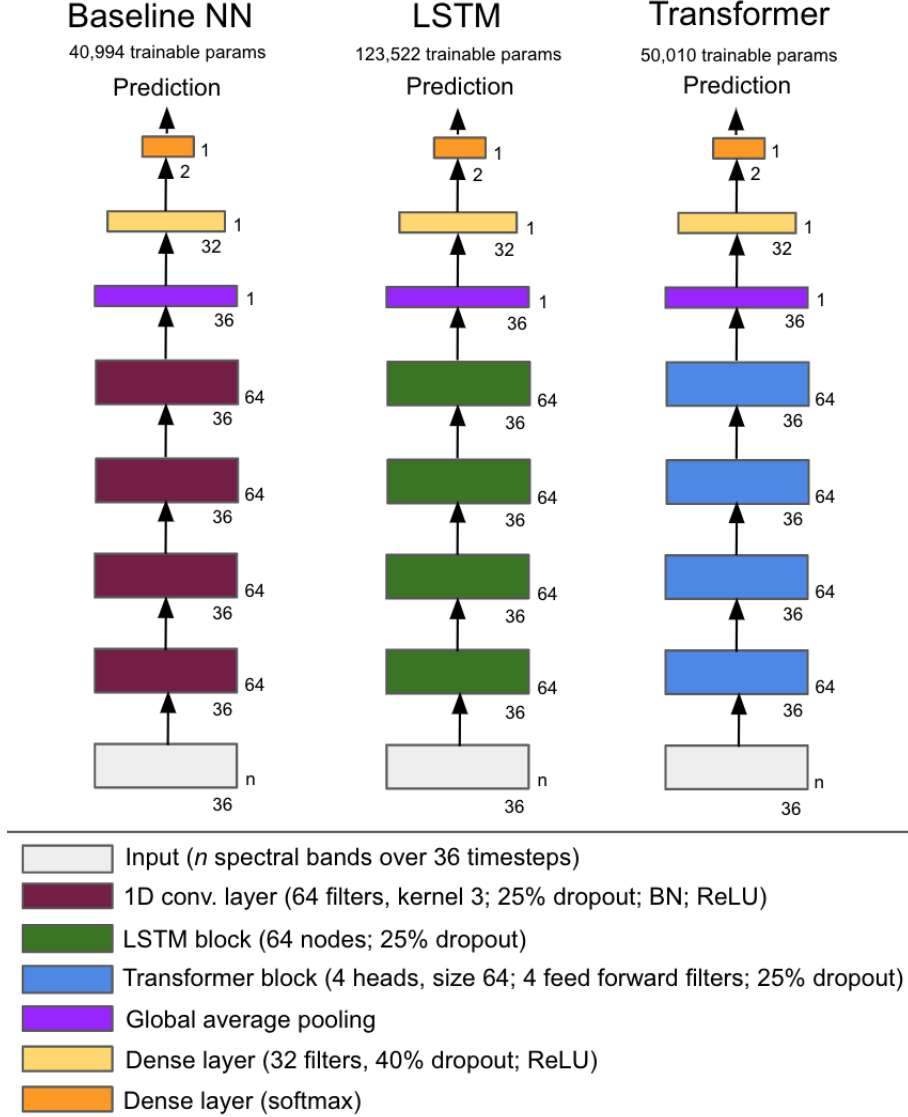


Figure 4: Neural network (NN) model architectures tested as irrigation detection classifiers. Model architectures are consistent by design; only encoding blocks differ across networks.

the number of samples for the region in question. Both class-balancing and region-balancing weights are used in all training configurations.

To address potential redundancy and time-specificity among samples within a region, random shifts are applied to all input timeseries. The sizes of these random shifts vary between -3 and +3 timesteps (corresponding to between -30 and +30 days), with an equal probability of all 7 possible shifts occurring (including a shift by 0 timesteps). Random shifts are applied to all samples in the training and validation sets and differ for each sample every time it's seen by the model. No shifts are applied to the samples in the testing sets.

The primary metric for performance evaluation is the F_1 score on the test datasets of regions withheld from training. Accordingly, performance is assessed in a manner that prioritizes classifier robustness – i.e. performance in regions unseen during training – and not in a manner that could be inflated by close similarity of samples within a region. For reference, the F_1 score balances prediction precision and recall, and is calculated per Eq. 1.

$$F_1 = \frac{TP}{TP + \frac{1}{2}(FP + FN)} \quad (1)$$

The training strategy differs for the tree-based classifiers and for the neural network-based classifiers. As training the tree-based classifiers occurs across a single batch with no iteration across epochs, there is no need for separate validation and testing datasets: The training and validation datasets of all included regions are therefore combined to create a single training dataset. After training on this combined dataset, performance is evaluated across the test datasets.

In contrast, training neural network-based models takes place by batch across epochs, and a validation set is required to guide the training process. For a given training step, one batch from each region is concatenated, with the combined output shuffled before model intake. After the epoch is finished, performance is assessed on the validation set of each region included in training. If the minimum F_1 score among all regions' validation sets has increased from its previous maximum, the model weights are saved; however, if the minimum F_1 score has not increased from its previous high point, the model weights are discarded. Minimum F_1 score across all validation regions is selected as the weight update criteria to ensure model robustness: Consistent performance across the entire area of interest is desired, not high performance in one set of regions and poor performance in another. Training concludes once the minimum validation region F_1 score has not improved for 10 training epochs, or after 30 epochs have been completed. After training, model weights are loaded from the epoch with the highest minimum validation region F_1 score; performance of this model on the test datasets of all regions is then reported. For all training runs, a binary cross-entropy loss, a learning rate of 1e-4, and an Adam optimizer [Kingma and Ba, 2015] are specified. Inputs are standardized to a mean of 0 and standard deviation of 1 using statistics from the entire set of labeled samples.

4 Results

4.1 Model sensitivity

Figure 5 presents withheld VC region test dataset F_1 scores for three different types of model input – one that includes all spectral bands for all timesteps; one that includes only the EVI layer for all timesteps; and one that includes only the EVI layer for all timesteps with the random sample shift applied. Here, the performance of models trained on all combinations of VC regions is evaluated; these results are organized along the x -axis by the number of VC regions included during training. Each x -axis tick label also includes in parentheses the number of withheld VC region test dataset evaluations, n , for all models trained on x included VC regions⁴. Mean and 10th percentile values of the n performance evaluations are displayed for each x between 1 and 6. All results are presented for the transformer model architecture; however, these findings are agnostic to the classifier architecture selected.

Figure 5 demonstrates that models trained on samples containing only EVI timeseries outperform those that include all spectral bands at all timesteps, both on average (a) and in low performing regions (b). The 10th percentile of withheld regions' F_1 scores is shown in order to understand the low-end of model performance without accounting for outliers. For reference, classifier performance based on the prediction admissibility criteria is also included. Figure 5 shows that explicitly feeding classification models information about samples' vegetation content – i.e. feature engineering – allows for better performance compared to models that intake 10 Sentinel-2 spectral bands. Introducing a random temporal shift to the EVI timeseries further increases performance; by increasing the sample variance seen by the model, randomly shifting the input timeseries improves model transferability. Supplementary Figure S4 provides additional evidence of the benefits of this training strategy: A gradient class-activation map shows that a classifier trained on randomly shifted timeseries better identifies dry season vegetation as predictive of irrigation presence.

Taken together, randomly shifted EVI timeseries increase withheld region F_1 scores by an average of 0.22 when only 2 VC regions are included in the training data, compared to models that use all spectral bands. As performance begins to plateau with 4 or more VC regions included in the training data, this gap shrinks to an improvement of 0.10. Similar results can be seen in Figure 5(b) for the low-end of performance: Extracting and randomly shifting EVI timeseries increase the 10th percentile of withheld region F_1 scores by 0.40 when 2 VC regions are included in the training data, a difference that shrinks to approximately 0.14 with 5 or more VC regions in the training data. Two additional findings are gleaned from the results for the models trained on randomly shifted EVI timeseries (i.e. the grey curve). First, a classifier trained on data from 2 VC regions or more outperforms the pixel filtering baseline. Second, increasing the number of VC regions included in the training set improves withheld region prediction performance up until 4 VC regions before tapering off.

⁴An example helps explain the calculation of n values: Given $x = 2$ VC regions included in training, there remain 5 VC regions unseen by the classifier. As there are $\binom{7}{2} = 21$ ways to select 2 VC regions from the full set of 7, and each of these combinations leaves 5 withheld VC regions for performance evaluation, $n = 105$ when $x = 2$.

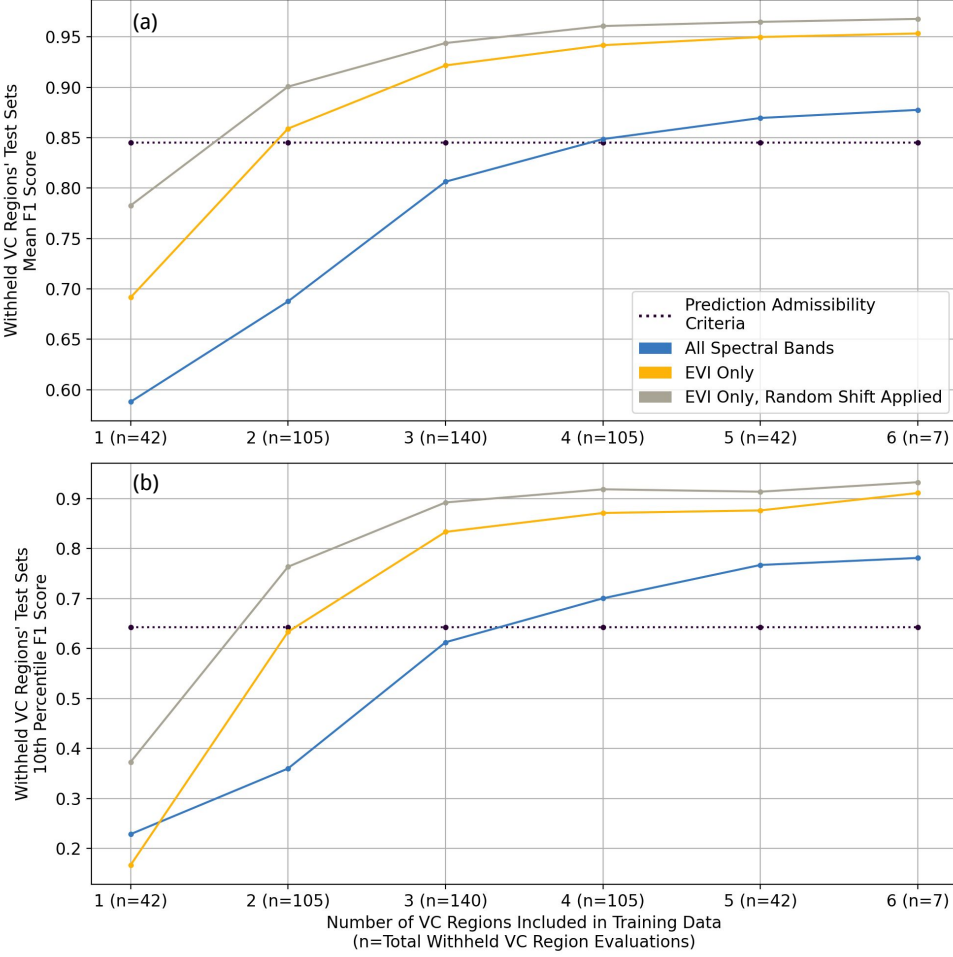


Figure 5: Withheld region test dataset performance for different types of model input, organized along the x-axis by the number of regions included during training. (a) presents mean F₁ score over the withheld regions; (b) presents the 10th percentile F₁ score over the withheld regions. Results indicate that model inputs of randomly shifted enhanced vegetation index (EVI) timeseries yield the best classifier performance. F₁ scores from classification based on the prediction admissibility criteria are presented for reference.

Figure 6 displays (a) mean and (b) 10th percentile F₁ score for all combinations of VC regions included in training for the 5 classification models tested, along with the reference classifier based on the prediction admissibility criteria. Figure 6 demonstrates that the transformer architecture is most robust for all combinations of VC training regions, followed closely by the CatBoost architecture for all training configurations with 2 or more VC regions. Moreover, for models with 5 or 6 VC regions included in training, mean and low-end F₁ scores for these two architectures are practically indistinguishable at 0.97 and 0.92, respectively. The Supplementary Materials contain further comparisons between Transformer and CatBoost performance (see Supplementary Table S6), showing that when each model is trained on all 7 VC regions' training data, the two models demonstrate an average regional prediction alignment of 98.9%. Moreover, an ablation study on training dataset size finds that reducing the proportion of polygons in the training set from 70% to 15% has minimal impact on prediction performance (See Supplementary Figure S5). Lastly, Figure 6 shows that the LSTM architecture does not noticeably improve performance compared to the baseline neural network, and that the trained Random Forest models yield the worst performance in withheld regions.

Next, prediction performance over the unseen ground-collected samples in Tana is assessed. As the transformer model demonstrates the most robust performance over withheld regions' samples, it is selected for prediction, achieving 96.7% accuracy over irrigated samples (88,128/91,898) and 95.9% accuracy over non-irrigated samples (33,954/35,121) for an F₁ score of 0.932. It is again worth noting that these high accuracies are achieved over the GC samples without the classification model seeing any labeled data from the Tana region during training.

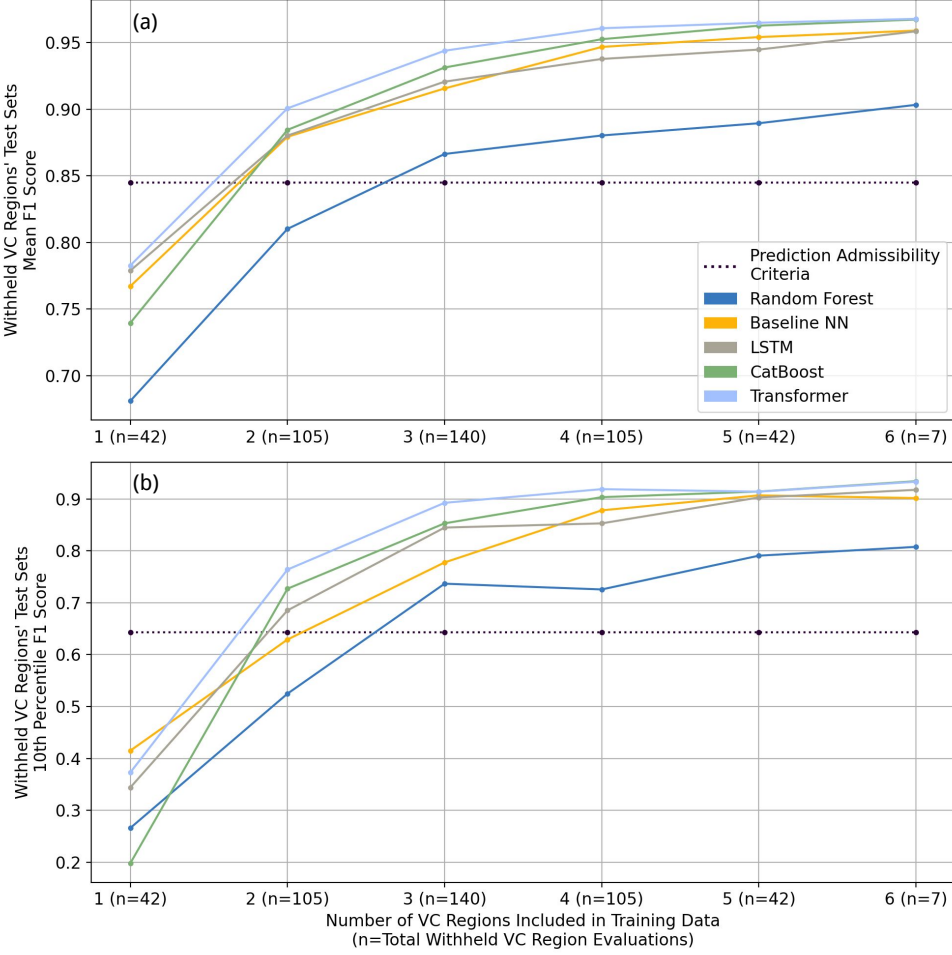


Figure 6: Withheld region test dataset performance for different classifier models, organized along the x -axis by the number of regions included during training. (a) presents mean F_1 score over the withheld regions; (b) presents the 10th percentile F_1 score over the withheld regions. Results indicate that the transformer based classifier yields the best performance, followed closely by the CatBoost model. F_1 scores from classification based on the prediction admissibility criteria are presented for reference.

4.2 Model inference

For model inference, the transformer architecture is trained on the randomly shifted EVI timeseries of the labeled data from the 7 VC and one GC regions. The trained model is then deployed over Tigray and Amhara for the 2020 and 2021 dry seasons (using imagery collected between June 1, 2019 and June 1, 2020; and between June 1, 2020 and June 1, 2021, respectively). Two post-processing steps are then taken: 1) the prediction admissibility criteria are applied, and 2) contiguous groups of predicted irrigated pixels smaller than 0.1 Ha are removed in order to ignore isolated, outlier predictions.

During inference, another step is taken to verify the accuracy of irrigation predictions. Here, five additional enumerators collect 1601 labeled polygons for the 2020 and 2021 dry seasons – 1082 non-irrigated polygons covering 3807 Ha and 519 irrigated polygons covering 582 Ha – across the extent of Amhara via the same labeling methodology used to collect the training, validation, and testing data. The locations of these independently labeled polygons are shown in Supplementary Figure S6. After cluster cleaning and applying the prediction admissibility criteria, these polygons yield 361,451 non-irrigated samples and 48,465 irrigated samples. An F_1 score of 0.917 is achieved over these samples – 98.3% accuracy over non-irrigated samples and 95.5% accuracy over irrigated samples, performance that remains in line with the reported test dataset metrics from Figure 6 and accuracies over the withheld Tana ground-collected labels.

Due to text constraints, Figures 7 and 8 present bitemporal irrigation maps at a resolution far coarser than their native 10m. The full resolution, georeferenced irrigation maps are available from the corresponding author upon request.

4.2.1 Tigray

Figure 7 presents predicted irrigated areas in Tigray for 2020 and 2021, with 2020 irrigation predictions in red and 2021 irrigation predictions in cyan. To better understand the nature of changing vegetation phenologies across this time period, the inset of Figure 7 contains example timeseries that produced an irrigation prediction in one of 2020 or 2021. These example timeseries show that a second crop cycle with vegetation growth peaking in January is associated with a positive irrigation prediction; in contrast, the non-existence of this cycle is associated with non-irrigated prediction. Table 2 displays the total predicted irrigated area for Tigray for 2020 and 2021, along with the total land area, organized by zone. Between 2020 and 2021, Table 2 quantifies a 39.8% decline in irrigated area in Tigray.

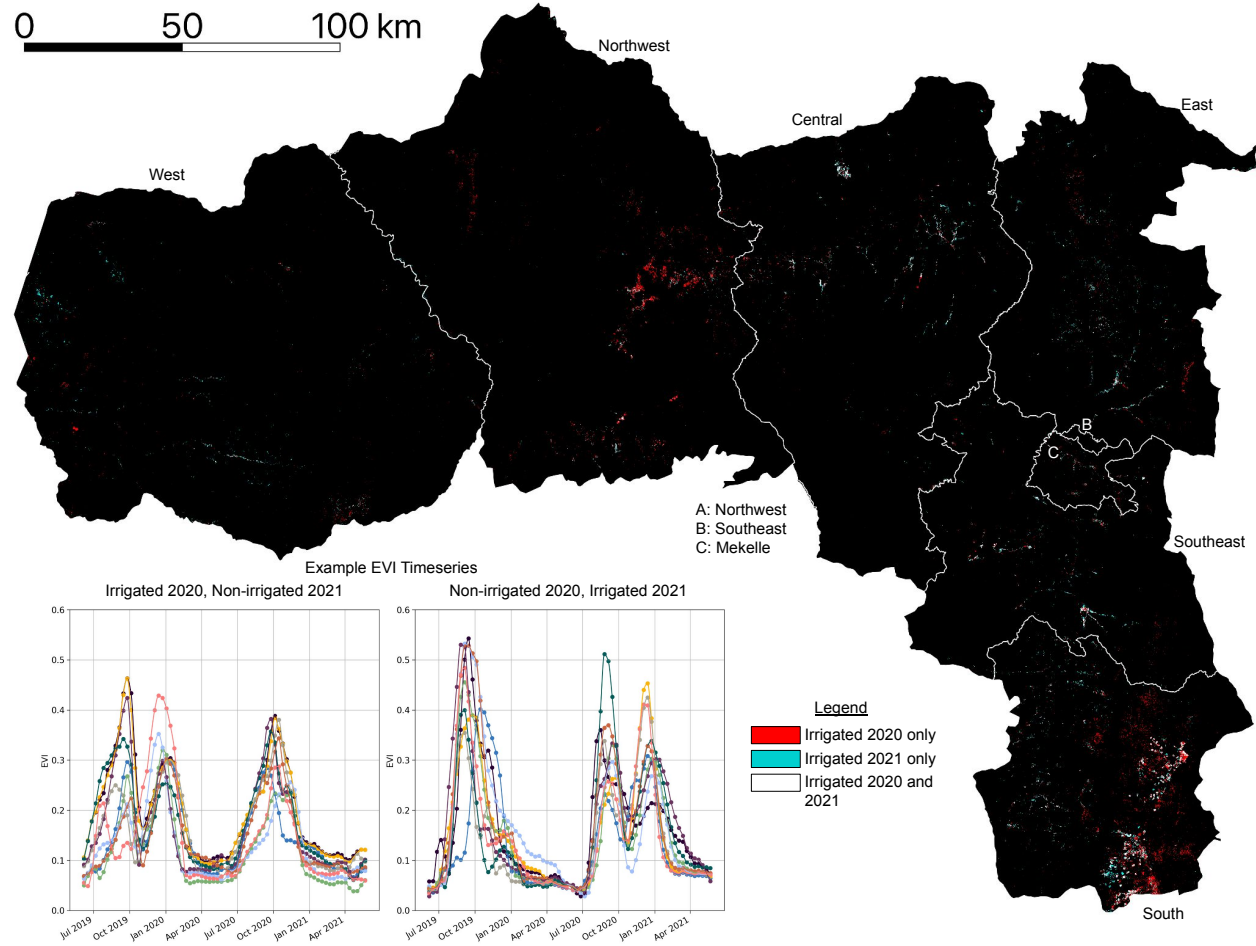


Figure 7: Bitemporal irrigation map for Tigray. Figure inset contains example EVI timeseries predicted as irrigated in either 2020 or 2021. A predominance of red indicates that many parts of Tigray contain irrigation detected in 2020 but not in 2021.

4.2.2 Amhara

Figure 8 presents a bitemporal irrigation map for Amhara, also with 2020 irrigation predictions in red and 2021 irrigation predictions in cyan. This map contains large clusters of irrigated predictions around Lake Tana in the zones of Central Gondar, South Gondar, and West Gojjam, an intuitive finding given the availability of water from Lake Tana and the rivers that extend off it. Irrigation is also detected in the portions of Amhara's easternmost zones that fall within the Main Ethiopian Rift (MER); as the valley formed by the MER extends north into Tigray, irrigation predictions in the North Wello, Oromia, and North Shewa zones align with irrigation predictions in the Southern zone of Tigray shown in

Table 2: Predicted irrigated area statistics in Tigray for 2020 and 2021, organized by zone.

Zone	Irrigated Ha., 2020	Irrigated Ha., 2021	Total Ha.	Percent Change, 2020 to 2021	Percent Change as Fraction of Total Area, 2020 to 2021
Central	3710	3554	954,616	-4.2%	0.0%
Eastern	3068	2863	635,670	-6.7%	0.0%
Mekelle	556	397	52,313	-28.5%	-0.3%
North Western	7439	2062	1,246,715	-72.3%	-0.4%
South Eastern	2658	2301	533,334	-13.4%	-0.1%
Southern	16,474	8064	506,151	-51.1%	-1.7%
Western	2278	2557	1,331,652	12.3%	0.0%
Total	36,181	21,799	5,260,451	-39.8%	-0.3%

Figure 7. Table 3 displays the total predicted irrigated area for Amhara for 2020 and 2021, along with the total land area, organized by zone. From 2020 to 2021, Table 3 quantifies a 41.6% decline in irrigated area in Amhara.

The inset of Figure 8 presents interannual irrigated cropping patterns for an area southwest of Choke Mountain. Interlocking red and cyan plots indicate the spatial rotation of irrigated crops from 2020 to 2021; no white plots are observed, which would signify dry season crop growth in both years.

Table 3: Predicted irrigated area statistics in Amhara for 2020 and 2021, organized by zone.

Zone	Irrigated Ha., 2020	Irrigated Ha., 2021	Total Ha.	Percent Change, 2020 to 2021	Percent Change as Fraction of Total Area, 2020 to 2021
awi	27,443	20,547	906,682	-25.1%	-0.8%
Central Gondar	73,450	50,954	2,095,018	-30.6%	-1.1%
East Gojjam	44,975	33,888	1,405,689	-24.7%	-0.8%
North Gondar	7381	3367	684,247	-54.4%	-0.6%
North Shewa (AM)	62,933	21,362	1,622,197	-66.1%	-2.6%
North Wello	21,367	8250	1,110,856	-61.4%	-1.2%
Oromia	30,875	5285	380,773	-82.9%	-6.7%
South Gondar	72,682	43,046	1,406,698	-40.8%	-2.1%
South Wello	28,215	16,302	1,849,812	-42.2%	-0.6%
Wag Hamra	447	698	890,004	56.4%	0.0%
West Gojjam	97,206	71,052	1,348,157	-26.9%	-1.9%
West Gondar	6180	1342	1,529,197	-78.3%	-0.3%
Total	473,155	276,093	15,229,329	-41.6%	-1.3%

5 Discussion

This manuscript makes a set of contributions to the literature for learning from limited labels. First, it demonstrates a process of collecting training data to supplement ground-collected labels that improves on previous methods of sample collection – such as using imagery from a single timestep or simple vegetation content heuristics – as it verifies the existence or non-existence of full vegetation cycles during the dry season. Second, an evaluation of inputs, classifier architectures, and training strategies is presented for achieving irrigation classifier applicability to a larger area. Results indicate that enhanced vegetation (EVI) timeseries outperform a full set of spectral bands as inputs; that randomly shifting input timeseries prevents classifier models from overfitting to region-specific input features; and that a transformer-based neural network produces the highest prediction accuracies in unseen target regions. Due to the close similarity of performance metrics and alignment of predictions, the faster training, more easily interpretable CatBoost architecture is also shown as a suitable alternative for irrigation mapping efforts.

Prediction results indicate strong classifier performance over sample timeseries from regions not seen during training. On data from withheld target regions, transformer-based classifiers achieve mean F_1 scores above 0.95 when four or more

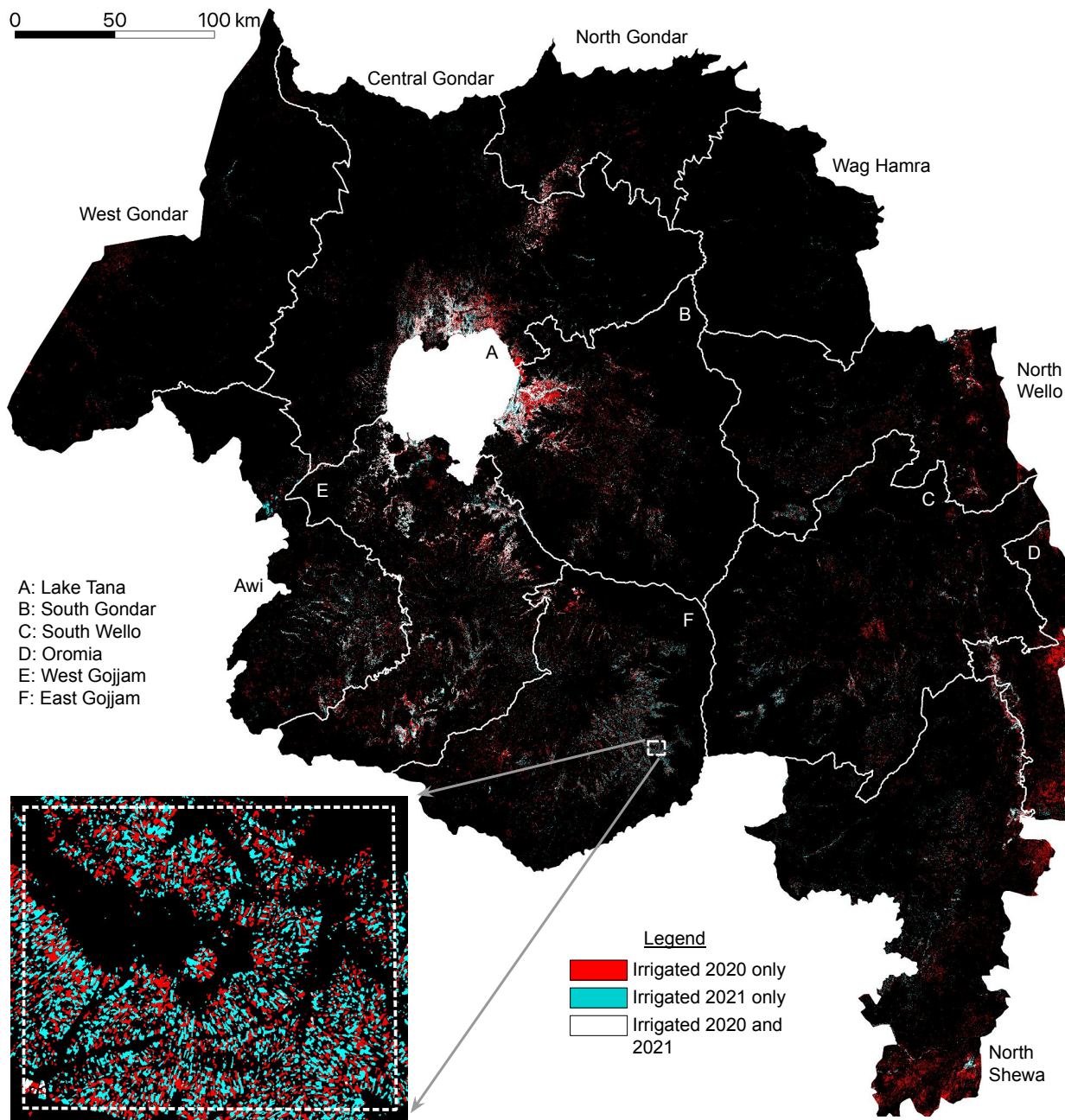


Figure 8: Bitemporal irrigation map for Amhara. Figure inset contains example predictions around Choke Mountain displaying interannual irrigation patterns. A predominance of red indicates that many parts of Amhara contain irrigation detected in 2020 but not in 2021.

regions' data are included during training; using labels from all 7 visual collection (VC) regions, the transformer-based classifier achieves an F_1 score of 0.932 on the ground collection (GC) labels around Lake Tana. Over an independently collected set of more than 400,000 samples collected for performance assessment, the same classifier achieves 98.3% accuracy over non-irrigated samples and 95.5% accuracy over irrigated samples, demonstrating strong performance throughout the entire Ethiopian highlands.

Deploying a transformer-based classifier trained on samples from all 8 label collection regions yields insight into changing irrigation patterns. Results suggest that from 2020 to 2021, irrigation in Tigray and Amhara decreased by 40%. In Tigray, this decline was most precipitous in the Northwest and Southern zones, which saw percent changes in

irrigated area of -72.3% and -51.1%, respectively. The Western zone of Tigray was the only zone to see an increase in irrigated area from 2020 to 2021; even so, this increase amounted to 279 Ha in a zone with a total area of 1,331,652 Ha. Amhara is predicted to have had similar decreases in irrigated area: Apart from the Wag Hamra zone, which was predicted to have less than 0.08% of its area irrigated in 2020 or 2021, all zones in Amhara experienced a change in irrigated area between -25.0% and -82.3%. The largest declines by area occurred in North Shewa (-41,572 Ha), South Gondar (-29,636 Ha), and West Gojjam (-26,154 Ha). Combined, results for Tigray and Amhara predict severe reductions in dry season crop growth from 2020 to 2021, findings that align with recent reports of food insecurity following the eruption of civil conflict in Ethiopia in late 2020.

Despite presented performance metrics indicating high levels of prediction accuracy, there are a few limitations to the proposed methodology that are important to mention. First, the study area is limited to the Ethiopian highlands, a highly agricultural, climatologically consistent area that is dominated by rainfed cropped phenologies. As the irrigation classifiers are only trained to separate dry season crop cycles from rainfed vegetation cycles – associating identified dry-season cropping with irrigation presence – they will perform poorly in settings with different rainfall and phenological patterns. Relatedly, the trained irrigation classifiers do not identify irrigation used to supplement rainy season precipitation, irrigation of perennial tree crops, evergreen vegetation in riparian areas, or irrigation that supports continuous cropping, as the phenological signatures of these types of vegetation are difficult to distinguish from evergreen, non-cropped signatures. This discrimination task is left for future work. Lastly, classifiers are trained only on cropped phenologies, which constitute a portion of the vegetation signatures that exist in the area of interest. To manage the other phenologies present at model inference, prediction admissibility criteria are implemented. Nevertheless, these criteria are imperfect: There are surely irrigated pixels which have been mistakenly assigned a non-irrigated class label, along with non-cropped pixels which have evaded the admissibility criteria.

While the presented methodology is applied only for the task of irrigation identification in the Ethiopian highlands, the strategy of regional phenological characterization to provide context for geographically informed selection of training samples and model applicability can be transferred more broadly to a range of land process mapping objectives. The suitability of this approach in the field of machine learning with limited labels is supported by results comparing classifier architectures and hyperparameter choice to assess the question of result uniqueness that overshadows all land cover classifications. As discussed by Small [2021], what is presented as *the* map is often just *a* map – one of many different products that can be obtained from the same set of inputs with different classifiers and hyperparameter settings. By assessing multiple classifier architectures and quantifying prediction sensitivity, this approach demonstrates consistency in results and indicates the uncertainty that can be expected of the resulting irrigation maps; as such, it provides a process for building robust classifiers in settings with scarce labeled data.

Conflict of Interest Statement

The authors declare that the research was conducted in the absence of any commercial or financial relationships that could be construed as a potential conflict of interest.

Author Contributions

TC and VM conceived of the study, which was led by VM. TC developed and implemented the methodology, analyzed the results, and produced the data visualizations. CS introduced the concept of multiscale phenological context and devised the spatiotemporal mixture model. VM consulted in all steps of these processes. TC is the primary author of the manuscript, which was prepared with editorial assistance from CS and VM.

Funding

Partial support for this effort was provided by the National Science Foundation (INFEWS Award Number 1639214), Columbia World Projects, Rockefeller Foundation (eGuide Grant 2018POW004), OPML UK (DFID) and Technoserve (BMGF).

Acknowledgments

The authors are grateful to Jack Bott, Yinbo Hu, Hasan Siddiqui, and Yuezi Wu for their assistance in labeling. The authors would like to thank Gunther Bensch (RWI), Andrej Kveder (OPML), Abiy Tamerat (EthioResource Group), Yifru Tadesse (ATA Ethiopia), and Esther Kim (Technoserve) for their assistance with field data collection efforts; Rose

Rustowicz for guidance in using of Descartes Labs platform; and colleagues Jay Taneja (UMass Amherst), Markus Walsh (AfSIS), and Edwin Adkins (Columbia) for their continued stimulating discussions and guidance.

Data Availability Statement

Labeled data and predicted irrigation maps are available from the corresponding author upon request.

References

- B. Abbasi, H. Arefi, B. Bigdeli, and S. Roessner. Automatic generation of training data for hyperspectral image classification using support vector machine. *International Archives of the Photogrammetry, Remote Sensing and Spatial Information Sciences - ISPRS Archives*, 40(7W3):575–580, 2015. doi:10.5194/isprsarchives-XL-7-W3-575-2015.
- B. Banerjee, F. Bovolo, A. Bhattacharya, L. Bruzzone, S. Chaudhuri, and B. K. Mohan. A new self-training-based unsupervised satellite image classification technique using cluster ensemble strategy. *IEEE Geoscience and Remote Sensing Letters*, 12(4):741–745, 2015. ISSN 1545598X. doi:10.1109/LGRS.2014.2360833.
- H. Bazzi, N. Baghdadi, I. Fayad, M. Zribi, H. Belhouchette, and V. Demarez. Near real-time irrigation detection at plot scale using sentinel-1 data. *Remote Sensing*, 12(9), 2020. ISSN 20724292. doi:10.3390/RS12091456.
- H. Bazzi, N. Baghdadi, G. Amin, I. Fayad, M. Zribi, V. Demarez, and H. Belhouchette. An operational framework for mapping irrigated areas at plot scale using sentinel-1 and sentinel-2 data. *Remote Sensing*, 13(13):1–28, 2021. ISSN 20724292. doi:10.3390/rs13132584.
- L. Breiman. Random Forests. *Machine Learning*, pages 1–28, 2001. doi:10.1201/9780429469275-8.
- Y. Chen, D. Lu, L. Luo, Y. Pokhrel, K. Deb, J. Huang, and Y. Ran. Detecting irrigation extent, frequency, and timing in a heterogeneous arid agricultural region using MODIS time series, Landsat imagery, and ancillary data. *Remote Sensing of Environment*, 204(March 2017):197–211, 2018. ISSN 00344257. doi:10.1016/j.rse.2017.10.030. URL <https://doi.org/10.1016/j.rse.2017.10.030>.
- T. Conlon, Y. Wu, C. Small, H. Siddiqui, E. Adkins, and V. Modi. A Novel Method of Irrigation Detection and Estimation of the Effects of Productive Electricity Demands on Energy System Planning. In *AGU Fall Meeting Abstracts*, volume 2020, pages GC034–08, Dec. 2020.
- R. P. de Lima and K. Marfurt. Convolutional neural network for remote-sensing scene classification: Transfer learning analysis. *Remote Sensing*, 12(1), 2020. ISSN 20724292. doi:10.3390/rs12010086.
- J. Deng, Wei Dong, R. Socher, Li-Jia Li, Kai Li, and Li Fei-Fei. ImageNet: A large-scale hierarchical image database. pages 248–255, 2009. doi:10.1109/cvprw.2009.5206848.
- A. V. Dorogush, A. Gulin, G. Gusev, N. Kazeev, L. O. Prokhorenkova, and A. Vorobev. Fighting biases with dynamic boosting. *CoRR*, abs/1706.09516, 2017. URL <http://arxiv.org/abs/1706.09516>.
- G. Gebregziabher, R. E. Namara, and S. Holden. Poverty reduction with irrigation investment: An empirical case study from Tigray, Ethiopia. *Agricultural Water Management*, 96(12):1837–1843, 2009. ISSN 03783774. doi:10.1016/j.agwat.2009.08.004.
- A. Huete, C. Justice, and W. Van Leeuwen. MODIS Vegetation Index (MOD13) algorithm theoretical basis document. 3(213):295–309, 1999.
- G. King and L. Zeng. Logistic regression in rare events data. *Political Analysis*, 9(2):137–163, 2001. ISSN 15487660. doi:10.18637/jss.v008.i02.
- D. P. Kingma and J. L. Ba. Adam: A method for stochastic optimization. *3rd International Conference on Learning Representations, ICLR 2015 - Conference Track Proceedings*, pages 1–15, 2015.
- Y. Lecun, Y. Bengio, and G. Hinton. Deep learning. *Nature*, 521(7553):436–444, 2015. ISSN 14764687. doi:10.1038/nature14539.
- Y. Li, H. Zhang, X. Xue, Y. Jiang, and Q. Shen. Deep learning for remote sensing image classification: A survey. *Wiley Interdisciplinary Reviews: Data Mining and Knowledge Discovery*, 8(6):1–17, 2018. ISSN 19424795. doi:10.1002/widm.1264.
- P. Naik and A. Kumar. *A Stochastic Approach for Automatic Collection of Precise Training Data for a Soft Machine Learning Algorithm Using Remote Sensing Images*. Springer Singapore, 2021. doi:10.1007/978-981-16-2712-5_24.
- M. Ozdogan, Y. Yang, G. Allez, and C. Cervantes. Remote sensing of irrigated agriculture: Opportunities and challenges. *Remote Sensing*, 2(9):2274–2304, 2010. ISSN 20724292. doi:10.3390/rs2092274.

- M. S. Pervez, M. Budde, and J. Rowland. Mapping irrigated areas in Afghanistan over the past decade using MODIS NDVI. *Remote Sensing of Environment*, 149:155–165, jun 2014. ISSN 0034-4257. doi:10.1016/J.RSE.2014.04.008.
- D. Phiri, M. Simwanda, S. Salekin, V. R. Nyirenda, Y. Murayama, and M. Ranagalage. Sentinel-2 data for land cover/use mapping: A review. *Remote Sensing*, 12(14), 2020. ISSN 2072-4292. doi:10.3390/rs12142291.
- C. A. Ramezan, T. A. Warner, A. E. Maxwell, and B. S. Price. Effects of training set size on supervised machine-learning land-cover classification of large-area high-resolution remotely sensed data. *Remote Sensing*, 13(3):1–27, 2021. doi:10.3390/rs13030368.
- S. Saha, Y. T. Solano-Correa, F. Bovolo, and L. Bruzzone. Unsupervised deep learning based change detection in Sentinel-2 images. *2019 10th International Workshop on the Analysis of Multitemporal Remote Sensing Images, MultiTemp 2019*, pages 0–3, 2019. doi:10.1109/Multi-Temp.2019.8866899.
- P. Sivaraj, A. Kumar, S. R. Koti, and P. Naik. Effects of Training Parameter Concept and Sample Size in Possibilistic c-Means Classifier for Pigeon Pea Specific Crop Mapping. *Geomatics*, 2(1):107–124, 2022. doi:10.3390/geomatics2010007.
- C. Small. Spatiotemporal dimensionality and Time-Space characterization of multitemporal imagery. *Remote Sensing of Environment*, 124:793–809, 2012. ISSN 00344257. doi:10.1016/j.rse.2012.05.031.
- C. Small. Grand Challenges in Remote Sensing Image Analysis and Classification. *Frontiers in Remote Sensing*, 1 (April):1–4, 2021. doi:10.3389/frsen.2020.605220.
- R. Stivaktakis, G. Tsagkatakis, and P. Tsakalides. Deep Learning for Multilabel Land Cover Scene Categorization Using Data Augmentation. *IEEE Geoscience and Remote Sensing Letters*, 16(7):1031–1035, 2019. ISSN 15580571. doi:10.1109/LGRS.2019.2893306.
- O. Stromann, A. Nascetti, O. Yousif, and Y. Ban. Dimensionality Reduction and Feature Selection for Object-Based Land Cover Classification based on Sentinel-1 and Sentinel-2 Time Series Using Google Earth Engine. *Remote Sensing*, 12(1), 2020. doi:10.3390/RS12010076.
- C. Tao, J. Qi, W. Lu, H. Wang, and H. Li. Remote sensing image scene classification with self-supervised paradigm under limited labeled samples. *CoRR*, abs/2010.00882, 2020. URL <https://arxiv.org/abs/2010.00882>.
- M. F. Vogels, S. M. de Jong, G. Sterk, and E. A. Addink. Mapping irrigated agriculture in complex landscapes using SPOT6 imagery and object-based image analysis – A case study in the Central Rift Valley, Ethiopia. *International Journal of Applied Earth Observation and Geoinformation*, 75(May 2018):118–129, 2019a. ISSN 1872826X. doi:10.1016/j.jag.2018.07.019.
- M. F. Vogels, S. M. de Jong, G. Sterk, H. Douma, and E. A. Addink. Spatio-temporal patterns of smallholder irrigated agriculture in the horn of Africa using GEOBIA and Sentinel-2 imagery. *Remote Sensing*, 11(2), 2019b. ISSN 20724292. doi:10.3390/rs11020143.
- M. T. Wakjira, N. Peleg, D. Anghileri, D. Molnar, T. Alamirew, J. Six, and P. Molnar. Rainfall seasonality and timing: implications for cereal crop production in Ethiopia. *Agricultural and Forest Meteorology*, 310:108633, 2021. ISSN 01681923. doi:10.1016/j.agrformet.2021.108633.
- Z. Wang, W. Yan, and T. Oates. Time series classification from scratch with deep neural networks: A strong baseline. *Proceedings of the International Joint Conference on Neural Networks*, 2017-May:1578–1585, 2017. doi:10.1109/IJCNN.2017.7966039.
- S. Wiggins, D. Glover, and A. Dorgan. Agricultural innovation for smallholders in sub-Saharan Africa. Technical Report July, 2021. URL <https://webarchive.nationalarchives.gov.uk/ukgwa/20211030121337/https://degrp.odi.org/publication/agricultural-innovation-for-smallholders-in-sub-saharan-africa/>.
- Y. Wu and L. S. Chin. A simplified training data collection method for sequential remote sensing image classification. *4th International Workshop on Earth Observation and Remote Sensing Applications, EORSA 2016 - Proceedings*, pages 329–332, 2016. doi:10.1109/EORSA.2016.7552823.
- X. Yu, X. Wu, C. Luo, and P. Ren. Deep learning in remote sensing scene classification: a data augmentation enhanced convolutional neural network framework. *GIScience and Remote Sensing*, 54(5):741–758, 2017. ISSN 15481603. doi:10.1080/15481603.2017.1323377.
- L. Zhong, L. Hu, H. Zhou, and X. Tao. Deep learning based winter wheat mapping using statistical data as ground references in Kansas and northern Texas, US. *Remote Sensing of Environment*, 233:111411, nov 2019. ISSN 0034-4257. doi:10.1016/J.RSE.2019.111411.

A MULTISCALE SPATIOTEMPORAL APPROACH FOR TRANSFERABLE IRRIGATION DETECTION

SUPPLEMENTARY MATERIALS

Terence Conlon*

Department of Mechanical Engineering
Columbia University
New York, NY, USA
terence.conlon@columbia.edu

Christopher Small

Lamont Doherty Earth Observatory
Columbia University
Palisades, NY, USA
csmall@columbia.edu

Vijay Modi

Department of Mechanical Engineering
Columbia University
New York, NY, USA
modi@columbia.edu

March 21, 2022

1 Supplementary Background

1.1 Phenology mapping by temporal endmember unmixing

Figure 1 in the main text presents a vegetation phenology map for Ethiopia created by applying a temporal mixture model to an image cube containing 16-day 250m MODIS enhanced vegetation index (EVI) imagery between June 1, 2011 and June 1, 2021. Figure S1 presents the locations of temporal endmember (tEM) extraction from the image cube transformed into principal component (PC) space. The four extracted tEMs are then used to create the phenology map via unconstrained least-squares linear unmixing per the methodology introduced in Small [2012].

Figure S2 presents the temporal mixture model inversion error and the cumulative error statistics for Figure 1. Interpreting Figure 1 and Figure S2 together reveals that the locations of highest error occur over evergreen vegetation, primarily in the southeast of Ethiopia. As the unmixing error remains low over Tigray and Amhara, the authors stipulate that Figure 1 contains an accurate assessment of vegetation cycles in the area of interest.

2 Supplementary Methods

2.1 Sentinel-2 imagery collection

Using the Descartes Labs platform, imagery mosaics are generating by collecting all Sentinel-2 imagery available within a 10-day timestep that come from 100km-by-100km granules with less than 10% aggregate cloud cover. These images are then sorted by cloud cover and masked using the cloud masks provided by the European Space Agency (ESA) Sen2Cor algorithm [Main-Knorn et al., 2017]. Given the 5-day revisit period of Sentinel-2 near the equator, a 10-day timestep ensures that there are two separate satellite passes per image mosaic.

Once imagery is collected for each timestep, values are assigned to individual pixels, pulling first from the image with the lowest amount of cloud cover. If there are masked pixels in this image, pixel values are determined for these locations using the image with the next lowest amount of cloud cover; this process repeats until either all the images available at a timestep are cycled through or each pixel in the 10-day mosaic is filled with valid, non-clouded values.

*Corresponding author

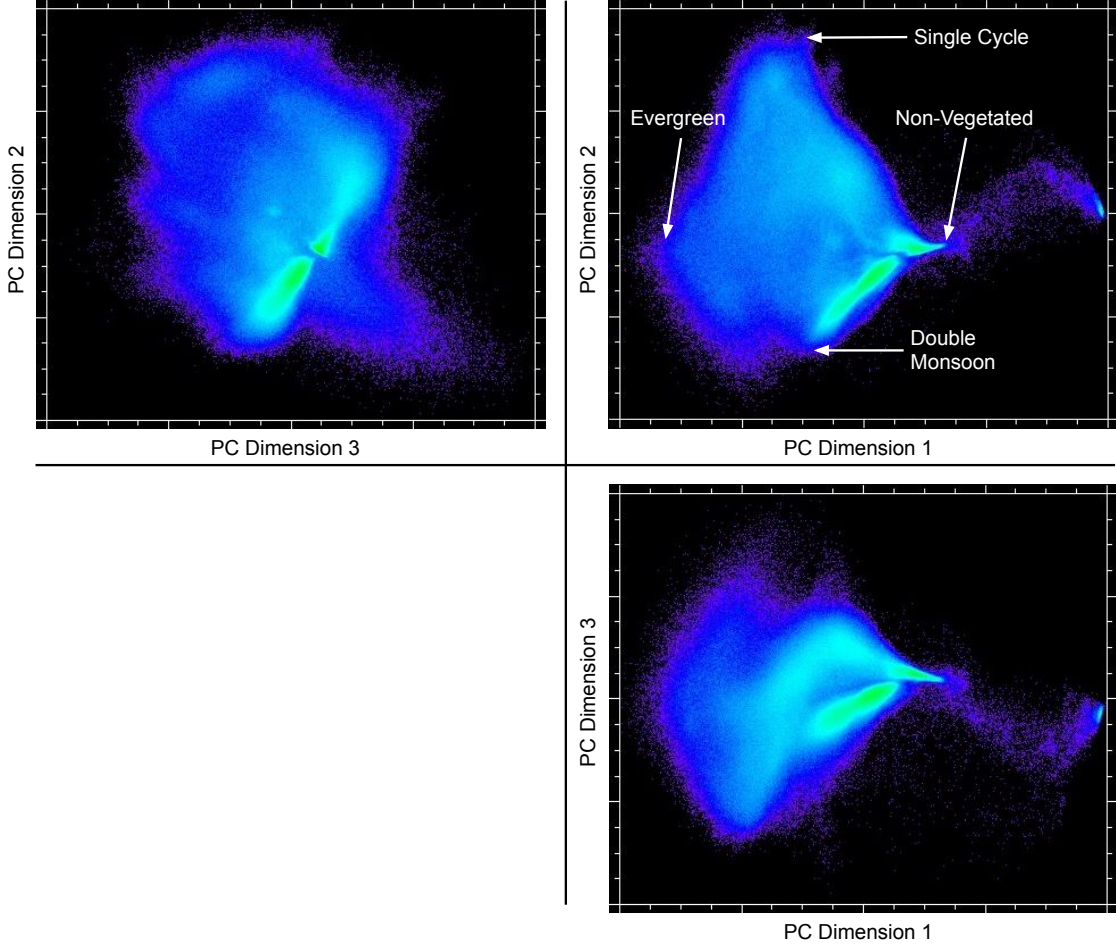


Figure S1: Views of the first three principal component (PC) dimensions of the transformed 10-year Ethiopia MODIS enhanced vegetation index (EVI) imagery cube. Locations of temporal endmembers used to construct the phenology map in Figure 1 via unconstrained linear unmixing are presented in the PC Dimension 1 vs. PC Dimension 2 plot.

For mosaics that retain invalid pixels due to persistent cloud cover across the timestep (often during the rainy season in Ethiopia, which stretches from June to September), pixel values are assigned via temporal interpolation: Each invalid pixel is given a linearly interpolated value based on the nearest preceding and subsequent image mosaic with a non-clouded value for that pixel.

Image mosaicking is performed bandwise. All 10m and 20m Sentinel-2 bands are extracted (10 bands in total); the 60m coastal aerosol and water vapor bands are ignored, as these bands contain atmospheric information not relevant for the land process monitoring task at hand. The final image processing step involves temporal smoothing of all timeseries using a 3rd order polynomial Savitzky-Golay filter with a window length of 5.

To assist with temporal interpolation of clouded pixels at the start and end of the specified time period, 82 image mosaics are collected in total – the 72 image mosaics that make up the 2 years of imagery (June 1, 2019 – June 1, 2020, and June 1, 2020 – June 1, 2021), plus 5 additional timesteps before and after the beginning and end of full time period. After interpolation and smoothing, these additional image mosaics are discarded to leave cloud-free, smoothed, 10 band Sentinel-2 imagery for only the desired 72 timesteps. The imagery is then split into annual temporal stacks, with all training and inference done on a single year's 36 timesteps of imagery.

Table S1 presents statistics on the amount of interpolation necessary to construct 10-day S2 timeseries for all of Tigray and Amhara in 2020 and 2021. Of the 18.94B pixel values in the annual EVI timeseries for Tigray, 15.8% are interpolated in 2020 and 18.3% are interpolated in 2021. In Amhara, more pixel values require interpolation due to more cloud cover: Of the 54.85B pixel values in the annual Amhara EVI timeseries, 29.6% are interpolated in 2020

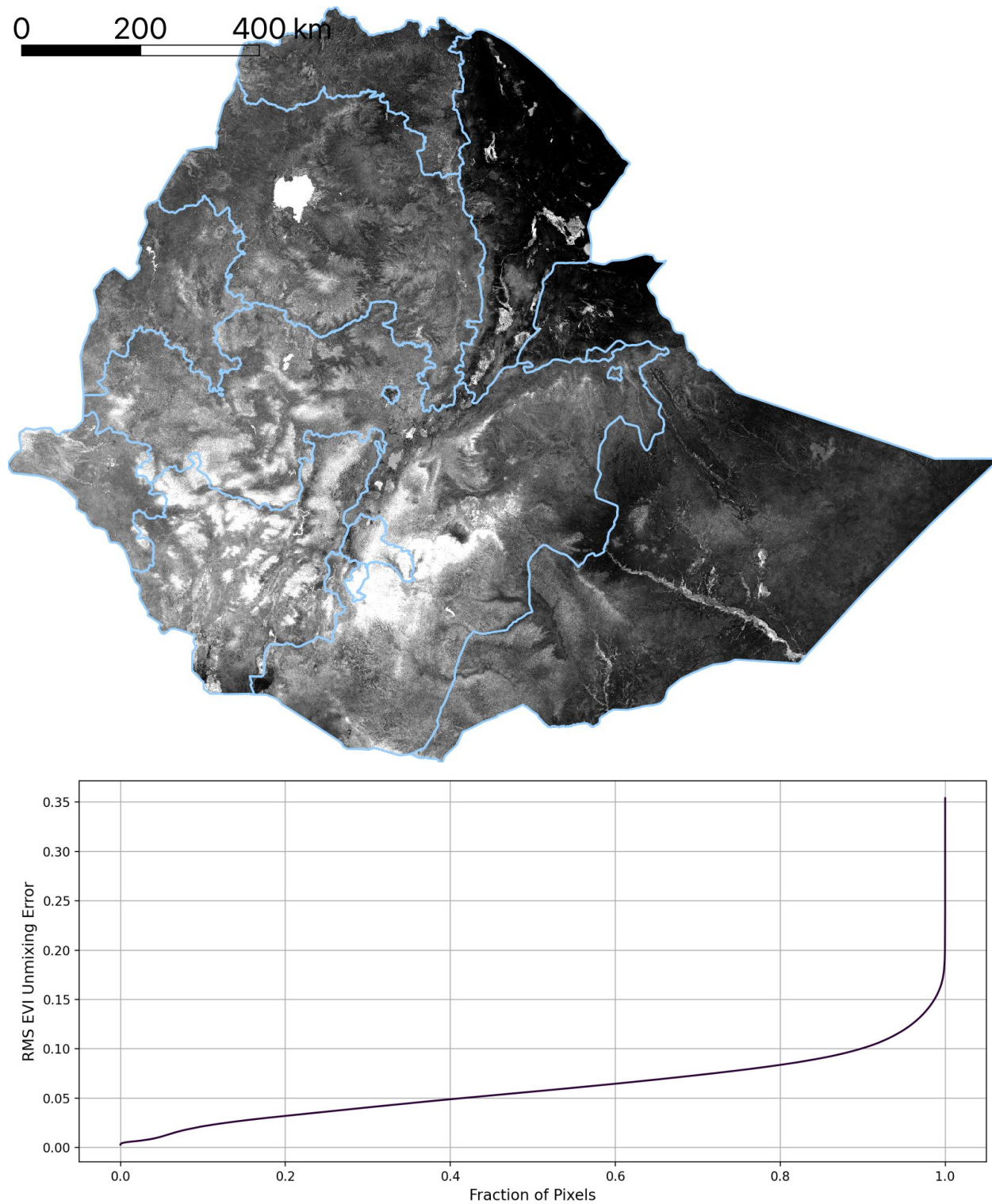


Figure S2: Root mean square (RMS) error of the temporal mixture model inversion for Figure 1. A 2% linear stretch is applied to the error map, with administrative boundaries outlined in light blue. The displayed cumulative density function shows the distribution of RMS errors for an increasing fraction of pixels in Figure 1.

and 25.2% are interpolated in 2021. In Tigray and Amhara, more than 95% of pixel interpolation in both years is a result of the 10% cloud cover threshold filtering out all imagery collected at a given timestep; the remaining <5% of interpolations occur for specific pixels deemed as clouds per the ESA Sen2Cor algorithm.

Intuitively, more pixels are interpolated during the Ethiopian Highlands' rainy season (Jun. 1 – Oct. 1) than during the dry season (Dec. 1 – Apr. 1), per Table S1. During the rainy months in Tigray, 32.7% of pixels are interpolated in 2020 and 44.7% of pixels are interpolated in 2021; for these same months in Amhara, 54.2% and 54.4% of pixels are interpolated in 2020 and 2021, respectively. While these fractions of interpolated pixels appear high, the authors note that EVI timeseries values during the rainy season are not highly predictive of dry season irrigation presence, and as such will have limited impact on classifier behavior. Instead, rainy season EVI values are used to inform the general characteristics of a year's vegetation timeseries, in particular to identify evergreen or barren land cover per the pixel admissibility criteria (see main text, Section 3.3). In contrast, less than 9% of dry season pixels in Tigray and Amhara are interpolated in both 2020 and 2021.

Table S1: Sentinel-2 imagery timeseries interpolation statistics.

	Total Fraction of Pixels Interpolated	Fraction of Pixels Interpolated Due to No Imagery at Timestep	Fraction of Pixels Interpolated in Rainy Season (Jun. 1 – Oct. 1)	Fraction of Pixels Interpolated in Dry Season (Dec. 1 – Apr. 1)
Tigray, 2020	0.158	0.954	0.327	0.064
Tigray, 2021	0.183	0.976	0.447	0.010
Amhara, 2020	0.296	0.972	0.542	0.088
Amhara, 2021	0.252	0.972	0.544	0.017

2.2 Ground collection

The ground collection survey was conducted during the months of March and April, 2021. Enumerators collected labels across an area north and east of Lake Tana (referred to as “Tana”; see Figure 1 in the main text) in a process that involved traveling to individual plots of lands, collecting four coordinate points corresponding to the corners of the plot, and specifying whether irrigation was present on the plot during the visit. The ground collection survey team collected 2002 polygons in Tana: 1500 were labeled non-irrigated and 502 were labeled irrigated. In total, these polygons cover 1867 Ha, 78% of which was designated as non-irrigated.

2.3 Labeled data accounting

Tables S2 and S3 present summaries of the number of labeled polygons and the number of labeled samples used in this paper's analysis.

2.4 Labeled data exploration

To better understand the vegetation phenologies contained within this study's labeled data, the similarities of EVI timeseries of the same class are explored across regions. This process first involves applying a PC transform to all labeled training data. The samples' dimensionality is then reduced by using only the first 10 dimensions of the transformed data; these first 10 dimensions explain 91% of the variance contained within the samples' EVI timeseries.

After dimensionality reduction via the PC transform, the two sample Kolmogorov-Smirnov (KS) test statistic is calculated between sample distributions of the same class across regions. The two-sample KS statistic determines the largest absolute distance between two 1D empirical distributions, and is presented in Eq. S1:

$$D_{KS} = \sup_x |F_1(x) - F_2(x)| \quad (\text{S1})$$

where F_1 and F_2 are the two empirical distribution functions of 1D variable x , and \sup is the supremum function. The KS statistic is assessed for two reasons: 1) the statistic depends on no assumptions about the underlying data distributions; and 2) the statistic has been adapted for multivariate distributions via the pseudo-1D KS metric [Hagen et al., 2020].

Table S2: Summary of labeled polygons, split by region and model training configuration. GC stands for ground collection labels; VC stands for visual collection labels.

Region	Type of Labels	Number of Labeled Polygons							
		Training		Validation		Testing		Total	
		Non-Irrig.	Irrig.	Non-Irrig.	Irrig.	Non-Irrig.	Irrig.	Non-Irrig.	Irrig.
Tana	GC	1050	351	225	76	225	75	1500	502
Rift	VC	12	25	3	6	3	6	18	37
Koga	VC	27	46	6	10	6	10	39	66
Kobo	VC	26	28	6	6	6	7	38	41
Alamata	VC	17	16	4	4	4	4	25	24
Liben	VC	24	25	5	5	6	6	35	36
Jiga	VC	15	13	4	3	3	3	22	19
Motta	VC	17	17	4	4	4	4	25	25
Total	GC + VC	1188	521	257	114	257	115	1702	750

Table S3: Summary of labeled samples, split by region and model training configuration. GC stands for ground collection labels; VC stands for visual collection labels.

Region	Type of Labels	Number of Labeled Samples							
		Training		Validation		Testing		Total	
		Non-Irrig.	Irrig.	Non-Irrig.	Irrig.	Non-Irrig.	Irrig.	Non-Irrig.	Irrig.
Tana	GC	63,729	24,675	14,283	5089	13,910	5361	91,922	35,125
Rift	VC	92,157	104,682	19,149	19,269	20,378	20,286	131,684	144,237
Koga	VC	150,378	98,697	29,661	23,015	27,953	24,401	207,992	146,113
Kobo	VC	93,838	123,946	30,549	36,494	31,473	48,077	155,860	208,517
Alamata	VC	58,310	21,176	14,356	4601	11,083	6447	83,749	32,224
Liben	VC	132,999	113,733	26,027	31,212	35,394	21,895	194,420	166,840
Jiga	VC	113,640	79,143	33,244	15,368	38,734	12,204	185,618	106,715
Motta	VC	94,153	47,915	34,267	11,127	27,568	9074	155,988	68,116
Total	GC + VC	799,204	613,967	201,536	146,175	206,493	147,745	1,207,233	907,887

In this adaptation, the pseudo-1D KS metric, $D_{KS,P1D}$, is the Euclidean KS statistic calculated between successive orthogonal dimensions of two multivariate distributions:

$$D_{KS,P1D} = \sqrt{(D_{KS,1})^2 + (D_{KS,2})^2 + \dots + (D_{KS,n})^2} \quad (\text{S2})$$

where

$$D_{KS,n} = \sup_{y_n} |F_1(y_n) - F_2(y_n)| \quad (\text{S3})$$

Here, Eq. S3 represents the KS statistic between the empirical distribution functions F_1 and F_2 of the n^{th} dimension of multivariate variable y . As only the first 10 PC dimensions of the transformed data are used, n ranges between 1 and 10.

Table S4 presents pairwise pseudo-1D KS statistics between regions' non-irrigated samples; Table S5 presents pairwise pseudo-1D KS distances between regions' irrigated samples. Here, the relative statistics between distributions are

Table S4: Pairwise pseudo-1D Kolmogorov-Smirnov (KS) statistics between regions' non-irrigated training samples. Values with typographical symbols are to be interpreted alongside Table S7.

	Tana	Rift	Koga	Kobo	Alamata	Liben	Jiga	Motta	Mean
Tana	0.00	1.13	1.85	1.00	1.25	1.69	1.50	1.33	1.39
Rift	1.13	0.00	1.48	0.62	0.71	1.43	0.95	0.57	0.98
Koga	1.85*	1.48	0.00	1.48	1.33	0.41	1.02	1.26	1.26
Kobo	1.00	0.62	1.48	0.00	0.76	1.45	1.16	0.91	1.05
Alamata	1.25	0.71	1.33	0.76	0.00	1.33	0.97	0.72	1.01†
Liben	1.69	1.43	0.41	1.45	1.33	0.00	0.91	1.23	1.21
Jiga	1.50**	0.95	1.02	1.16	0.97	0.91	0.00	0.51	1.00
Motta	1.33	0.57	1.26	0.91	0.72	1.23	0.51	0.00	0.93‡
									1.11

Table S5: Pairwise pseudo-1D Kolmogorov-Smirnov (KS) statistics between regions' irrigated training samples. Values with typographical symbols are to be interpreted alongside Table S7.

	Tana	Rift	Koga	Kobo	Alamata	Liben	Jiga	Motta	Mean
Tana	0.00	1.88	2.25	1.73	1.65	1.13	1.60	1.27	1.64
Rift	1.88	0.00	1.48	0.61	0.37	2.01	1.30	1.51	1.31
Koga	2.25*	1.48	0.00	1.37	1.45	2.46	1.98	2.20	1.88
Kobo	1.73	0.61	1.37	0.00	0.65	1.98	1.51	1.57	1.35
Alamata	1.65	0.37	1.45	0.65	0.00	1.78	1.11	1.31	1.19†
Liben	1.13	2.01	2.46	1.98	1.78	0.00	1.41	0.98	1.68
Jiga	1.60**	1.30	1.98	1.51	1.11	1.41	0.00	0.89	1.40
Motta	1.27	1.51	2.20	1.57	1.31	0.98	0.89	0.00	1.39‡
									1.48

compared, as the absolute statistics cannot be interpreted in a physically meaningful way. The cells with typographical marks in the two tables indicate statistics to be interpreted with the results in Table S7, discussed alongside that table. Tables S4 and S5 show that the relative pairwise statistic between regional distributions is larger among the irrigated sample sets, indicating that irrigated samples are more dissimilar across regions compared to the non-irrigated samples. This takeaway reflects the varying nature of irrigation practices across Ethiopia – irrigation can occur at different parts of the dry season for a variety of different crops. In contrast, the phenologies of non-irrigated cropland must mirror Ethiopia's primary rains, which are consistent in time for the regions included in this analysis.

2.5 Determining the prediction admissibility criteria

The prediction admissibility criteria presented in the Methodology of the main text (see Table 1) are informed by the cumulative distribution functions (CDFs) of the collected samples' EVI timeseries. By imposing admissibility criteria that closely match the distribution of the samples' EVI timeseries, heuristics are devised to exclude many pixels not relevant to the non-irrigated/irrigated cropland prediction methodology. Figure S3 presents CDFs for the 10th and 90th EVI timeseries percentiles, the 90th:10th EVI timeseries percentile ratio, and the maximum EVI value during the dry season. Values are presented for all regions' irrigated samples only, along with a set of pixel timeseries over evergreen areas.

Figure S3(a) shows that a maximum of 0.2 for the 10th percentile of the EVI timeseries is achieved by nearly all irrigated samples, and how this ceiling filters out 85% of all evergreen samples. Similarly, a minimum 90th:10th percentile EVI

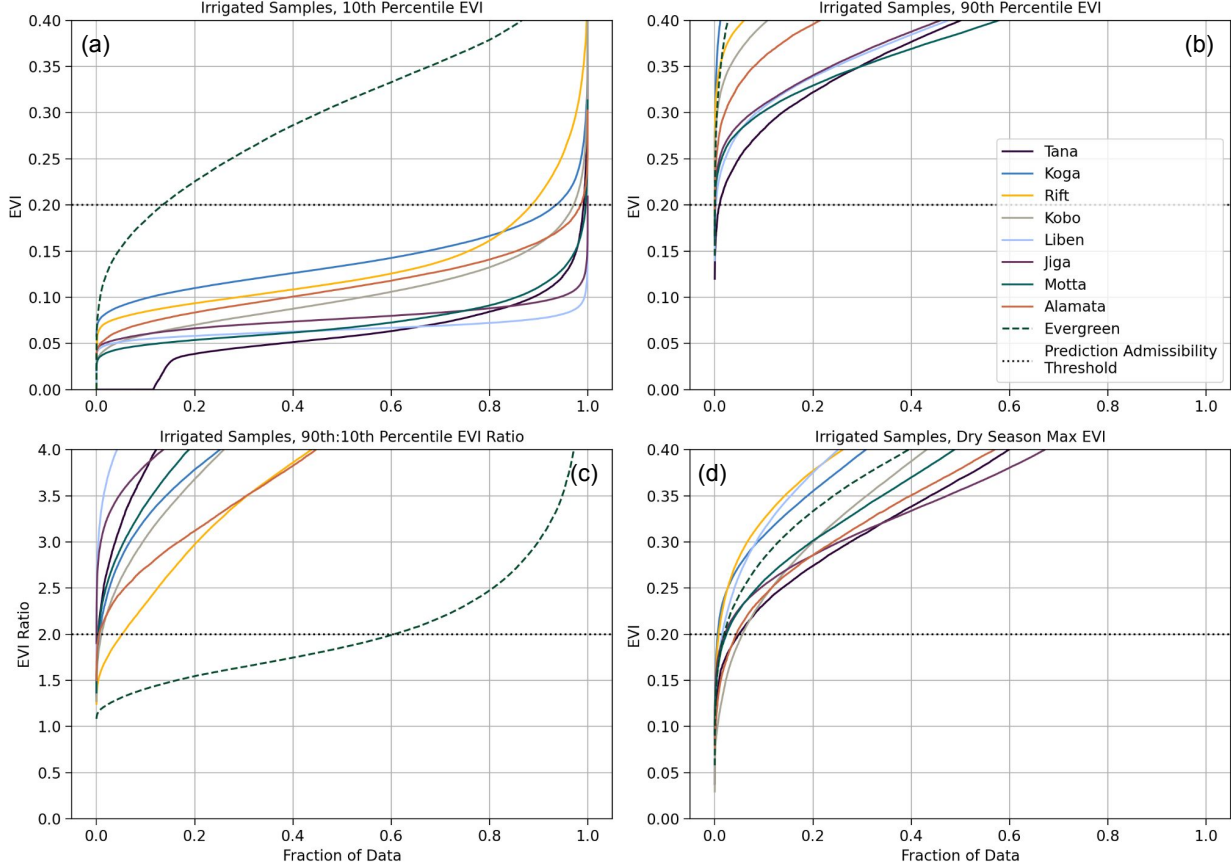


Figure S3: Cumulative distribution functions (CDFs) for the (a) 10th and (b) 90th EVI timeseries percentiles; (c) the 90th:10th EVI timeseries percentile ratio; and (d) the maximum EVI value during the dry season (December 1st, 2020, to April 1st).

ratio of 2 is satisfied by nearly all irrigated samples and excludes 60% of evergreen samples (Figure S3(c)). While no EVI timeseries for barren or non-vegetated areas are shown in this figure, the criteria specifying a 90th percentile EVI value above 0.2 and a dry season max EVI value above 0.2 are met by the vast majority of irrigated samples (Figure S3(b,d)), and would filter out many of these non-cropped pixels.

3 Supplementary Results

3.1 Evaluating the effects of randomly shifted input timeseries with a Gradient-Class Activation Map

Implementing a modified Gradient-Class Activation Map (Grad-CAM) for visual prediction explanation provides further evidence for improved prediction robustness from randomly shifting input EVI timeseries. A Grad-CAM uses the gradients flowing into the final layer of a neural network to produce a localization map highlighting important portions of the input for predicting a concept. Originally developed for images in Selvaraju et al. [2020], this technique can be applied analogously to timeseries. To do so, a transformer-based classifier model with its 32-node penultimate dense layer removed is trained on all VC regions' training datasets; by removing this fully connected layer, the importance of each timestep input for prediction can be visualized, as there is no longer a layer obscuring the gradient flow into the final prediction nodes. Figure S4 displays the normalized timestep prediction importances for 16 randomly selected non-irrigated and irrigated EVI timeseries from the Koga region. Results are presented for two models: the first trained without randomly shifting input timeseries, and the second trained with the random shift applied.

Figure S4 demonstrates that the input timesteps most important for prediction – displayed in red per the Normalized Logit Importance colorbar – are more continuous and better reflect a common understanding of what portions of a

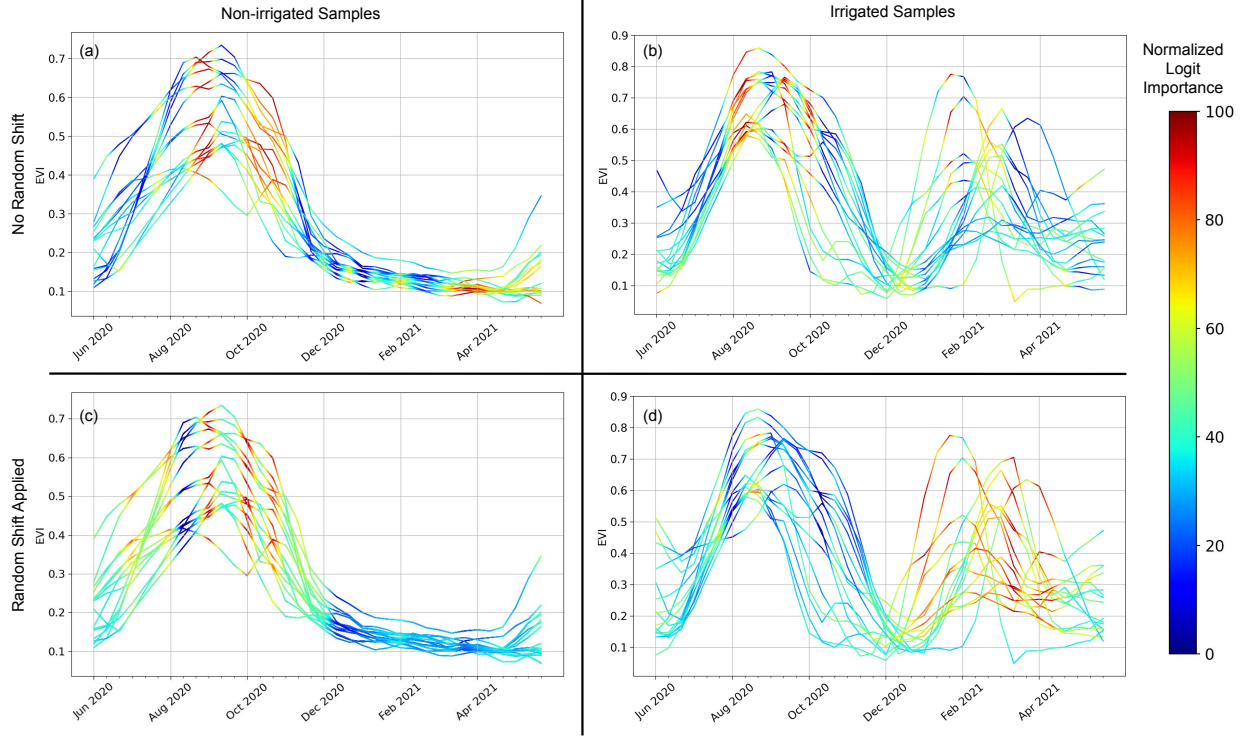


Figure S4: Modified Grad-CAM timestep importances for 16 randomly selected non-irrigated and irrigated enhanced vegetation index (EVI) timeseries from Koga, before and after the timeseries shift is applied.

phenology should be predictive once the model is trained on randomly shifted input timeseries. For the non-irrigated samples, the model trained on the randomly shifted timeseries identifies a larger portion of the timesteps during the rainy season as highly predictive (Figure S4(c)); this model also correctly identifies vegetation growth during dry season timesteps as important for identifying irrigated samples (Figure S4(d)). In comparison, the model trained on the non-shifted timeseries identifies scattered timesteps as predictive for both non-irrigated and irrigated samples (Figure S4(a,b)); it does not emphasize dry season vegetation growth as predictive of irrigation presence (Figure S4(b)). Instead, this model learns to identify isolated, non-intuitive timesteps, and as a consequence is more likely to misclassify input timeseries that differ slightly from those in the training data.

3.2 Ablation study: Limiting polygons used during training

To understand the impact of the amount of training data on model performance, an ablation study is conducted where the fraction of labeled polygons included in each region’s training dataset is varied between 0.15 and 0.85; the complementary fraction of each region’s polygons comprises the test dataset. For each fraction of training polygons, the CatBoost model architecture is trained on all combinations of all 7 visual collection (VC) regions’ training datasets; performance is assessed on the withheld VC regions in a process identical to the one described for main text Figures 5 and 6. All models are trained on randomly shifted EVI timeseries.

Figure S5 presents the results of this ablation study, in which minimal impact is observed when varying the fraction of polygons included in each region’s training dataset between 0.15 and 0.85. On average, withheld region F1 score decreases by approximately 0.05 as the fraction of training polygons drops from 0.85 to 0.15 when 1 VC region is included in the training data; this gap shrinks as additional VC regions are incorporated during training, becoming negligible for all models trained on 3 or more VC regions’ data. A larger performance delta among the 10th percentile of withheld regions’ F1 scores exists when fewer than 3 VC regions are included during training; similar to the average performance metrics, this gap collapses when the classification model is trained on labeled data from 3 or more VC regions.

Figure S5 demonstrates that the irrigation prediction models are robust even when limiting the fraction of polygons included in training datasets to 15% of the total. Here, the inclusion of labeled data from multiple regions and randomly

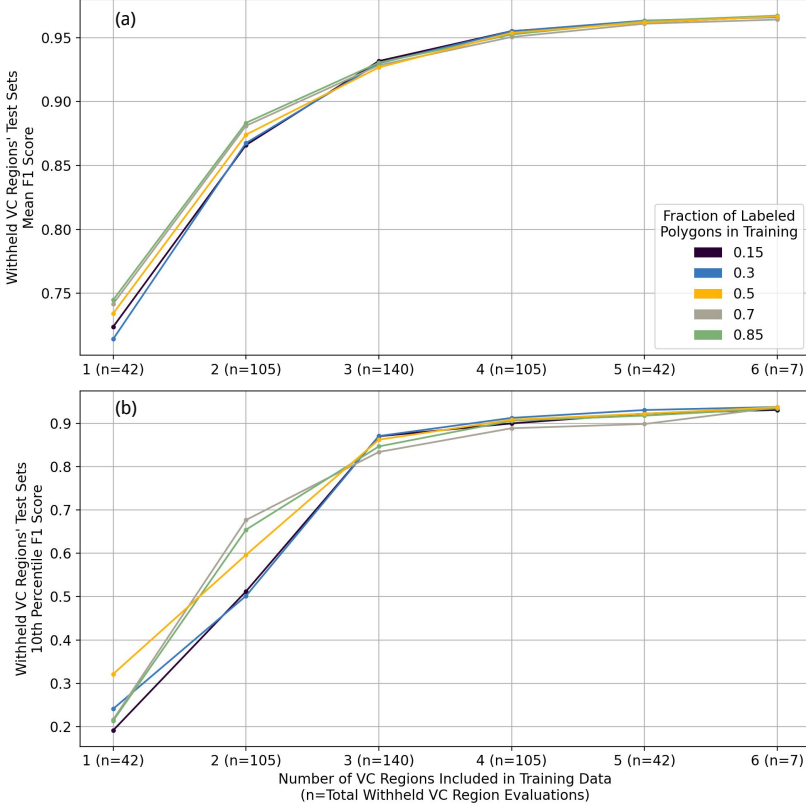


Figure S5: Withheld region test dataset performance for different fractions of labeled polygons included in the training datasets; the complementary fractions of labeled polygons constitute the test datasets. Predictions are made using a CatBoost model architecture. (a) presents mean F1 score over the withheld regions; (b) presents the 10th percentile F1 score over the withheld regions.

shifting the EVI timeseries inputs introduces enough variance to the classification model during training so that performance over regions unseen by the classifier remains high.

3.3 Comparison of predictions across model architectures

To ensure that different irrigation detection architectures converge on similar decision boundaries, the alignment of predictions across the transformer-based and CatBoost models is investigated. Here, both architectures are trained on the randomly shifted EVI timeseries of all 7 VC regions' training datasets; predictions are then made over all labeled samples. Table S6 presents the alignment of these predictions, showing a high degree of prediction similarity: An average regional prediction alignment of 98.9% is calculated. The close alignment of predictions made by both these models expands the basis for the solution set.

3.4 Determining the relative importance of each visual collection region

Through a pair of ordinary least-squares (OLS) regressions, the contribution of each VC region to target region performance can be assessed. Table S7 presents OLS regression coefficients and P-values on target region F1 scores for the 7 VC regions used during training, where the F1 scores are collected over all withheld regions for all transformer classifier models presented in Figure 6 of the main text. In interpreting the regression results, variables with P-values above 0.05 are considered not statistically significant.

Table S7 shows that training data from the regions of Alamata or Kobo have the largest impact on Tana test dataset performance, increasing F1 score on average by 0.032 or 0.024, respectively. The non-statistically significant contributions of Koga and Jiga's training data to Tana test dataset performance are highlighted, shown by the values marked with * and **. Comparing these non-statistically significant results with the relevant cells in Tables S4 and S5 – also marked

Table S6: Comparison between Transformer and CatBoost model predictions for models trained on all 7 visual collection (VC) regions' training datasets.

Region	Type of Labels	Num. Aligned Sample Predictions		Num. Misaligned Sample Predictions		Fraction of aligned predictions
		Non-Irrig. (0)	Irrig. (1)	Transformer: 0 CatBoost: 1	Transformer: 1 CatBoost: 0	
Tana	GC	88,587	35,035	728	2690	0.973
Rift	VC	130,399	142,114	2367	1024	0.988
Koga	VC	207,536	144,284	1401	827	0.994
Kobo	VC	156,946	203,510	2313	583	0.992
Alamata	VC	84,024	31,978	615	251	0.993
Liben	VC	193,428	165,933	884	971	0.995
Jiga	VC	184,116	106,384	955	833	0.994
Motta	VC	155,056	65,956	1689	1363	0.986

with * and ** – reveals that non-irrigated and irrigated samples from both Koga and Jiga are more dissimilar from Tana labeled samples compared to the regional average, determined by the KS distance between the regions' data.

Table S7: Ordinary least squares regression on withheld target region F1 scores. F1 scores are collected over all withheld regions for all transformer classifier models presented in Figure 6 of the main text. Values with typographical symbols are to be interpreted alongside Tables S4 and S5.

Source VC Region	Tana (R ² =0.317, n=127)		Withheld VC Regions (R ² =0.18, n=441)	
	Coefficient	P-value	Coefficient	P-value
Rift	0.018	0.008	-0.012	0.327
Koga	0.013*	0.056*	0.016	0.172
Kobo	0.024	0.001	0.029	0.016
Alamata	0.032	0.000	0.071†	0.000†
Liben	-0.011	0.122	0.028	0.019
Jiga	0.013**	0.063**	0.047	0.000
Motta	0.016	0.024	0.080‡	0.000‡

Table S7 also shows that the inclusion of labeled samples from Motta and Alamata during training causes the largest increase in F1 score over the withheld VC regions; these increases, shown by values marked with † and ‡, amount to 0.08 and 0.071, respectively. Again, comparing these data points to the KS distances marked with † and ‡ in Tables S4 and S5 demonstrates that non-irrigated and irrigated samples from Motta and Alamata are more similar to withheld VC regions' labeled data on average, as compared to samples from other VC regions.

Taken together, the results from Tables S4, S5, and S7 yield the intuitive finding that labeled samples more similar to those in a target region have a greater positive impact on performance, while more dissimilar labeled samples have a weaker effect on performance.

3.5 Independently labeled polygons for performance assessment at inference

Figure S6 presents the centroids of all polygons collected by additional enumerators for prediction performance assessment at model inference. Non-irrigated polygon locations are shown in red and irrigated polygons locations are shown in blue.

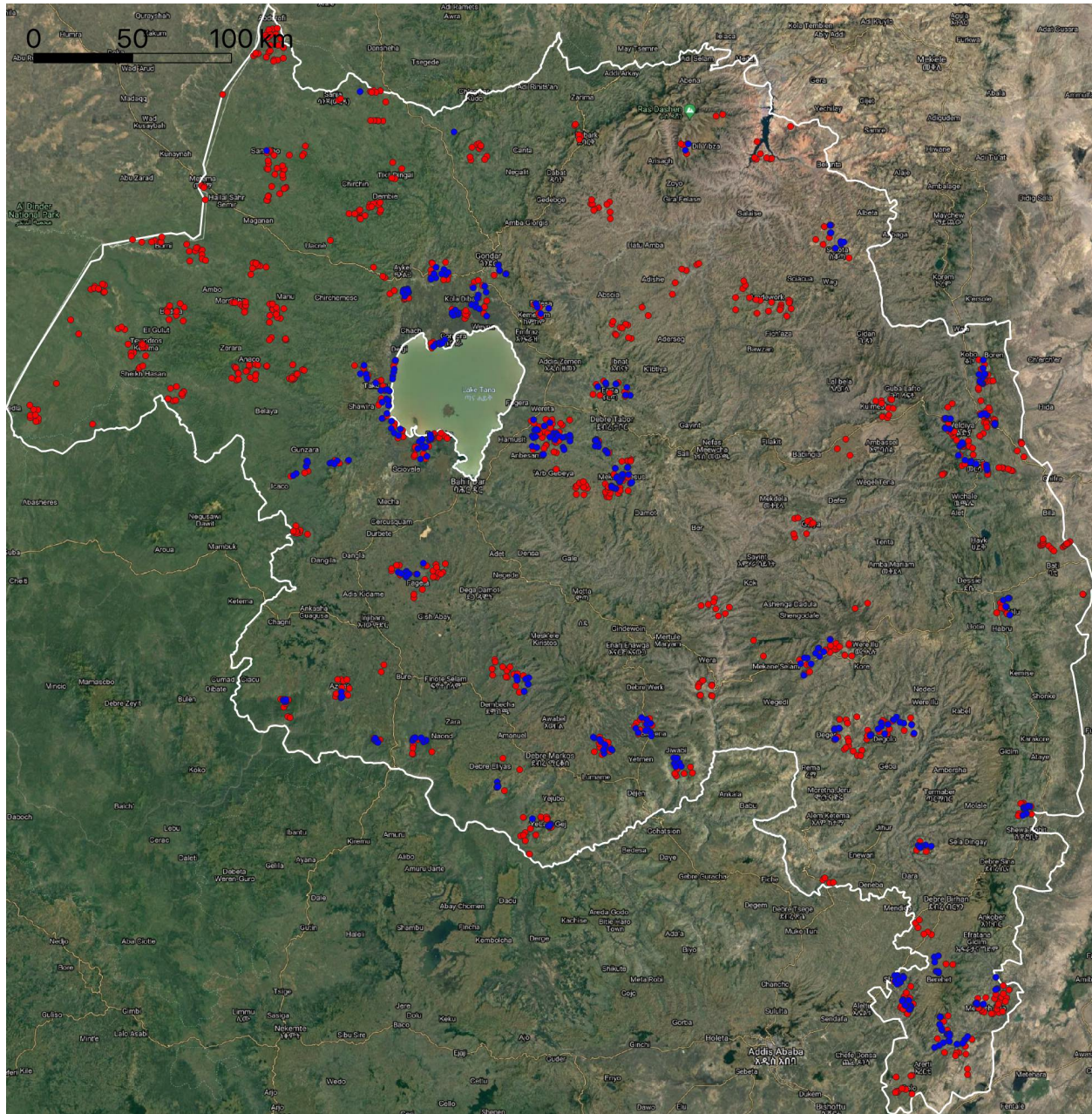


Figure S6: Locations of independently labeled polygons for additional model performance assessment. The centroids of non-irrigated polygons are shown in red, 1082 in total; the centroids of irrigated polygons are shown in blue, 519 in total. These polygons produce 361,451 non-irrigated samples and 48,465 irrigated timeseries samples.

References

- A. Hagen, J. Strube, I. Haide, J. Kahn, S. Jackson, and C. Hainje. A Proposed High Dimensional Kolmogorov-Smirnov Distance. *Machine Learning and the Physical Sciences: Workshop at the 34th Conference on Neural Information Processing Systems (NeurIPS)*, (NeurIPS):1–6, 2020. URL <https://ml4physicalsciences.github.io/2020/>.
- M. Main-Knorn, B. Pflug, J. Louis, V. Debaecker, U. Müller-Wilm, and F. Gascon. Sen2Cor for Sentinel-2. In L. Bruzzone, editor, *Image and Signal Processing for Remote Sensing XXIII*, volume 10427, pages 37–48. International Society for Optics and Photonics, SPIE, 2017. doi:10.1117/12.2278218. URL <https://doi.org/10.1117/12.2278218>.

R. R. Selvaraju, M. Cogswell, A. Das, R. Vedantam, D. Parikh, and D. Batra. Grad-CAM: Visual Explanations from Deep Networks via Gradient-Based Localization. *International Journal of Computer Vision*, 128(2):336–359, 2020. ISSN 15731405. doi:10.1007/s11263-019-01228-7.

C. Small. Spatiotemporal dimensionality and Time-Space characterization of multitemporal imagery. *Remote Sensing of Environment*, 124:793–809, 2012. ISSN 00344257. doi:10.1016/j.rse.2012.05.031.

Appendix A

Appendix A presents labeled samples before and after cluster cleaning for all label collection regions except Koga, which is presented in Figure 3 of the main text.

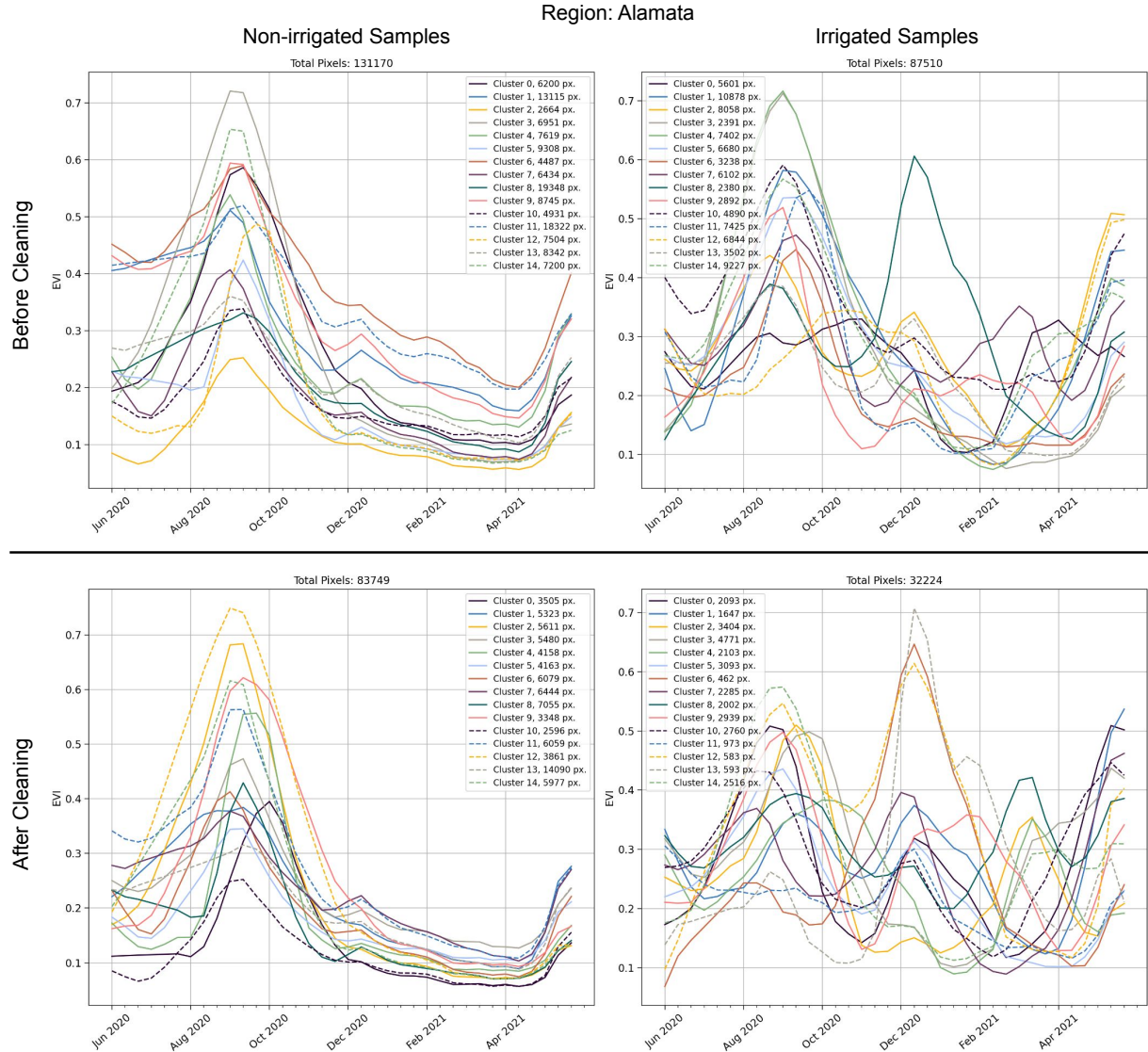


Figure S7: Clustered enhanced vegetation index (EVI) timeseries before and after cluster cleaning for the Alamata region. After cleaning, all non-irrigated clusters display a single vegetation peak aligned with the main rainy season, and the irrigated clusters all display a vegetation cycle during the dry season.

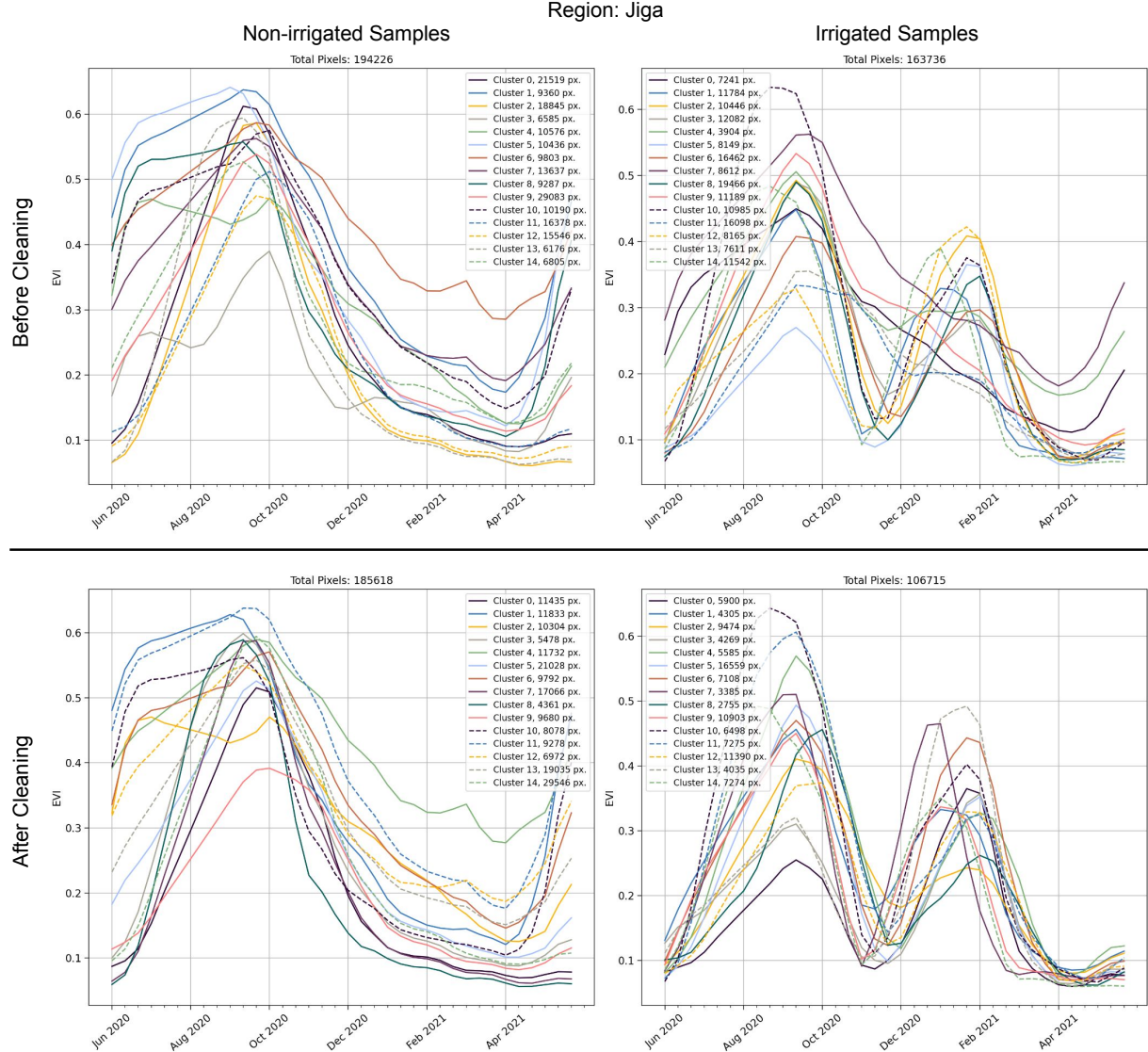


Figure S8: Clustered enhanced vegetation index (EVI) timeseries before and after cluster cleaning for the Jiga region. After cleaning, all non-irrigated clusters display a single vegetation peak aligned with the main rainy season, and the irrigated clusters all display a vegetation cycle during the dry season.

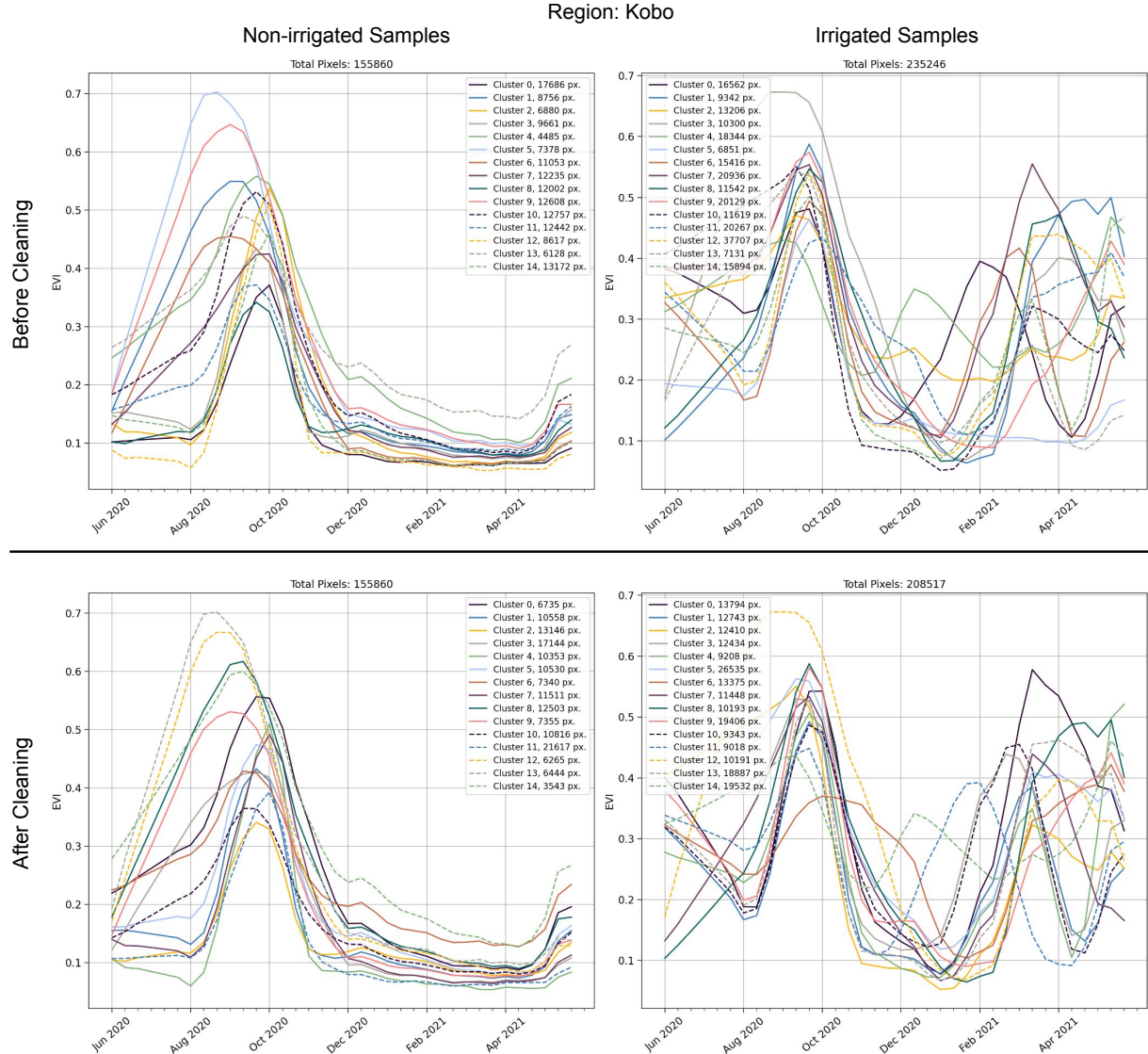


Figure S9: Clustered enhanced vegetation index (EVI) timeseries before and after cluster cleaning for the Kobo region. After cleaning, all non-irrigated clusters display a single vegetation peak aligned with the main rainy season, and the irrigated clusters all display a vegetation cycle during the dry season.

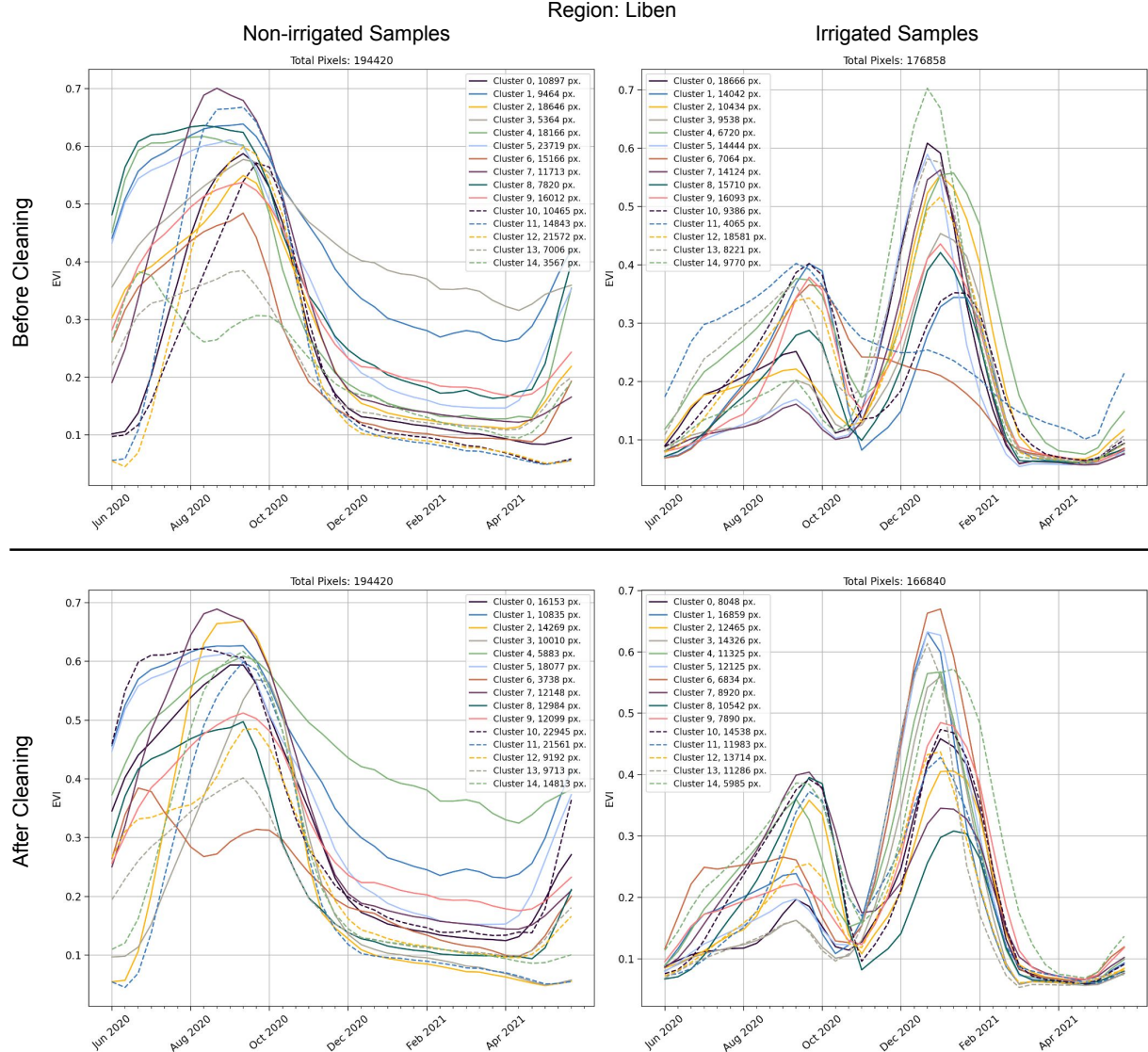


Figure S10: Clustered enhanced vegetation index (EVI) timeseries before and after cluster cleaning for the Liben region. After cleaning, all non-irrigated clusters display a single vegetation peak aligned with the main rainy season, and the irrigated clusters all display a vegetation cycle during the dry season.

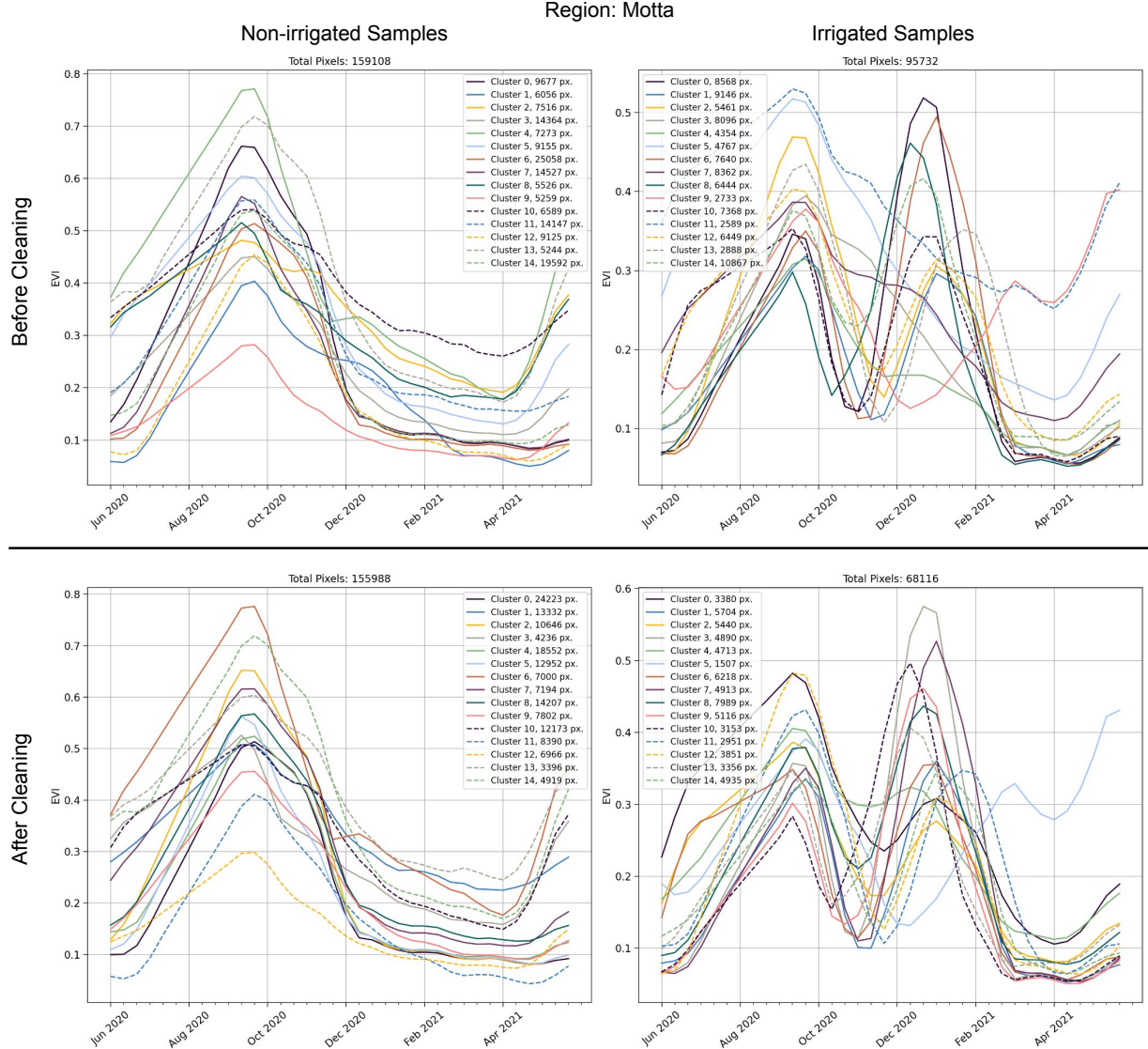


Figure S11: Clustered enhanced vegetation index (EVI) timeseries before and after cluster cleaning for the Motta region. After cleaning, all non-irrigated clusters display a single vegetation peak aligned with the main rainy season, and the irrigated clusters all display a vegetation cycle during the dry season.

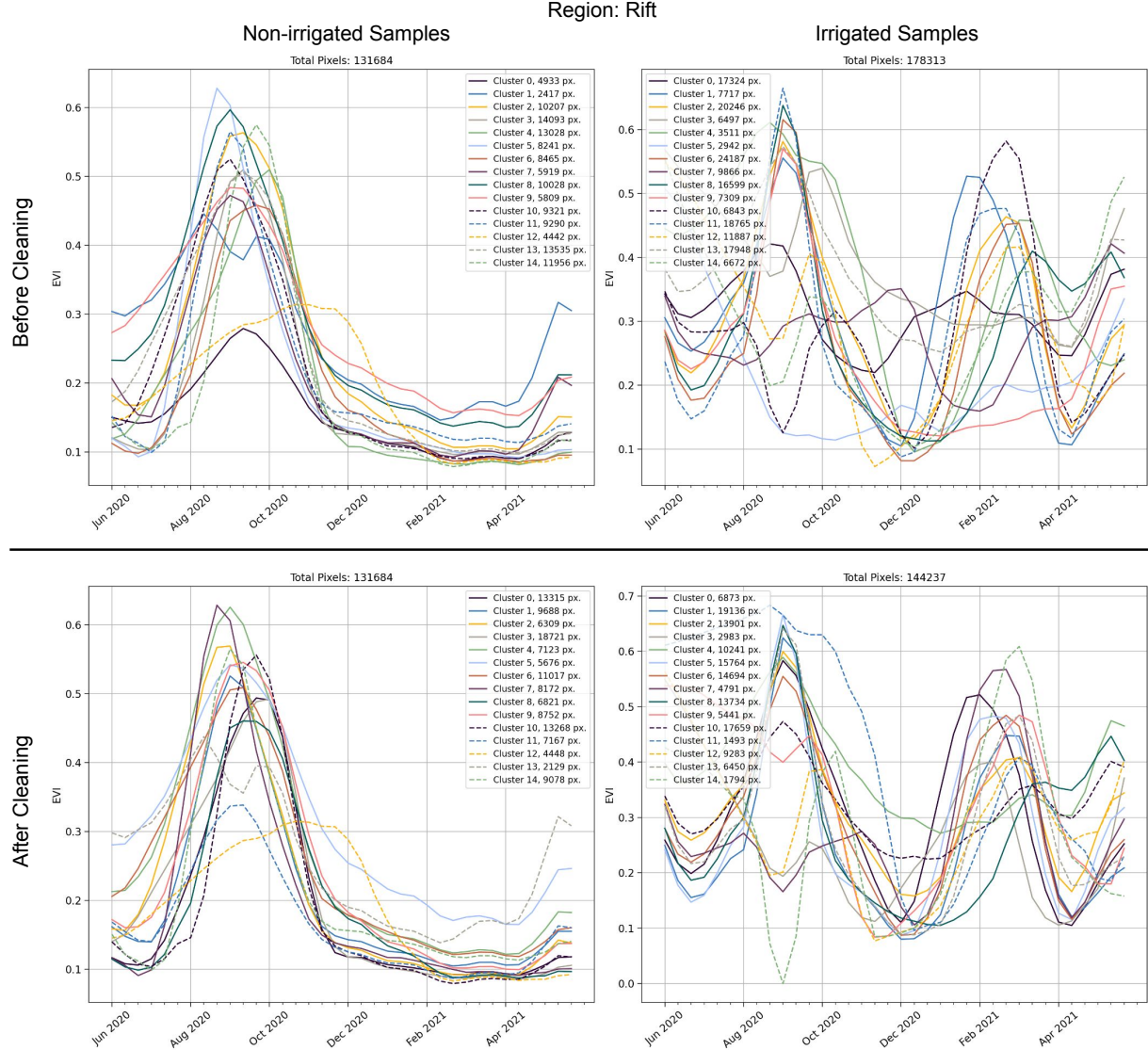


Figure S12: Clustered enhanced vegetation index (EVI) timeseries before and after cluster cleaning for the Rift region. After cleaning, all non-irrigated clusters display a single vegetation peak aligned with the main rainy season, and the irrigated clusters all display a vegetation cycle during the dry season.

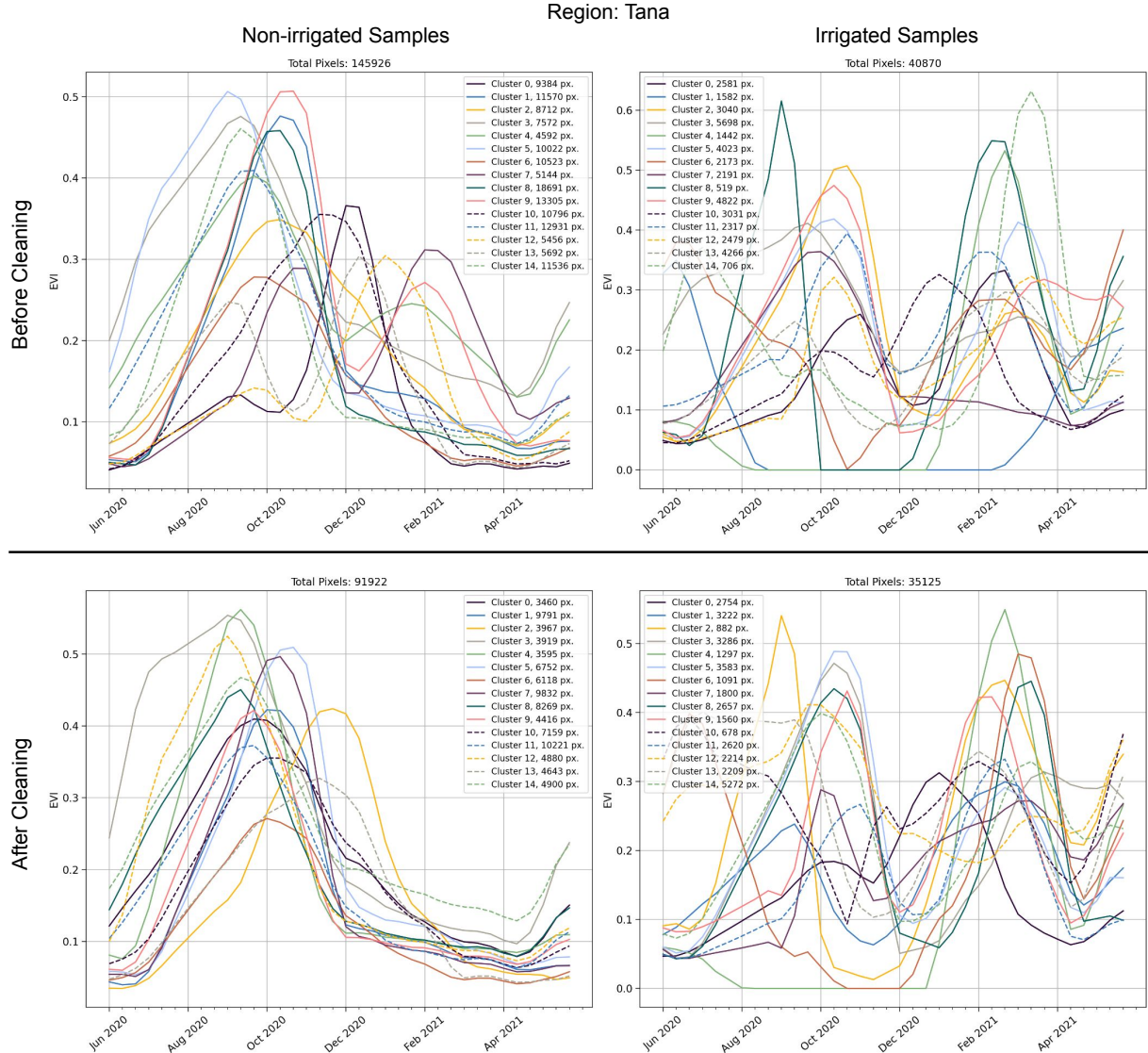


Figure S13: Clustered enhanced vegetation index (EVI) timeseries before and after cluster cleaning for the Tana region. After cleaning, all non-irrigated clusters display a single vegetation peak aligned with the main rainy season, and the irrigated clusters all display a vegetation cycle during the dry season.